ISIJ International, Vol. 65 (2025), No. 4, pp. 471–488
https://doi.org/10.2355/isijinternational.ISIJINT-2024-398

Review

Overview of ε-Martensite-Related Damage Evolution and its Solution: Pathways for Local Stress Accommodation, Plastic Damage Retardation, and Microcrack Arrest

Motomichi KOYAMA[1)]* and Takahiro SAWAGUCHI[2)]

1) Institute for Materials Research, Tohoku University, Katahira 2-1-1, Aoba-ku, Sendai, Miyagi, 980-8577 Japan.
2) National Institute for Materials Science, Sengen 1-2-1, Tsukuba, Ibaraki, 305-0047 Japan.

(*Received December 26, 2024; Accepted February 18, 2025; Advance online published March 5, 2025; Published April 15, 2025*)

The γ-ε martensitic transformation in austenitic steels generally enhances work hardening capacity and fatigue resistance. However, it also induces brittle-like fracture and compromises resistance to hydrogen embrittlement. Understanding the evolution mechanisms of plasticity, stress, and damage during deformation involving γ-ε martensitic transformation is essential to mitigate these adverse effects. To facilitate this understanding, this study reviews the mechanisms of stress concentration and accommodation, identifies cracking and crack arrest sites, and analyzes fracture behaviors associated with γ-ε martensitic transformation under monotonic tensile deformation and cyclic loading conditions. Furthermore, potential strategies for enhancing damage tolerance are introduced.

KEY WORDS: γ-ε martensitic transformation; work hardening; damage; austenitic steel; plastic anisotropy.

1. Introduction: Transformation-induced Stress and Damage

Deformation-induced martensitic transformation in certain steels serves as a significant mechanism of plasticity, contributing to shape memory properties[1)] and enhanced work-hardening capacity.[2,3)] In particular, the enhancement of work hardening capability owing to martensitic transformation is recognized as a critical factor in achieving substantial improvement of uniform elongation by suppressing macroscopic plasticity localization,[2,3)] a phenomenon referred to as the transformation-induced plasticity (TRIP) effect. The mechanisms responsible for work hardening in TRIP effects can be categorized into three primary factors: (1) the formation of matrix/martensite interfaces, which act as barriers to dislocation motion; (2) the formation of hard martensite, leading to stress partitioning; and (3) the development of plastically anisotropic martensite, which restricts slip transfer under specific crystallographic conditions. With respect to the interface effect, local transformation creates interfaces that inherently inhibit dislocation motion, even when there is no significant change in the physical or mechanical properties between the matrix and the martensite. This phenomenon is analogous to discussions on work hardening associated with deformation twinning, also known as the twinning-induced plasticity effect.[4,5)] The hardening mechanism driven by an increase in interface density with strain, which decreases effective grain size, is referred to as the dynamic Hall-Petch effect. The second factor, the hardness difference between martensite and the matrix, is generally discussed for an effect of martensitic transformation from face-centered cubic (FCC, γ) to body-centered cubic or body-centered tetragonal (BCC or BCT, α') structures in steels, particularly in the presence of significant carbon content. This hardness difference not only increases resistance to slip transfer from the matrix to martensite[6)] but also enhances stress partitioning,[7)] which increases work hardening. The third factor, the plastic anisotropy effect, is particularly important for non-cubic structures such as hexagonal close-packed (HCP) martensite that is referred to as ε-martensite in steels (*e.g.*, **Fig. 1**[8)]). When the critical resolved shear stress of the formed martensite exhibits high anisotropy, slip transfer from the matrix to the martensite, as well as subsequent dislocation motion within the martensite, becomes challenging under specific crystallographic orientation relationships among the matrix, martensite, and loading direction. This occurs even if the average hardness of the martensite is relatively low.[9)] Consequently, the combination of the three factors improves work hardening capability and uniform elongation in some optimal conditions.

Despite the effectiveness of both γ-α' and γ-ε martensitic

* Corresponding author: E-mail: motomichi.koyama.c5@tohoku.ac.jp

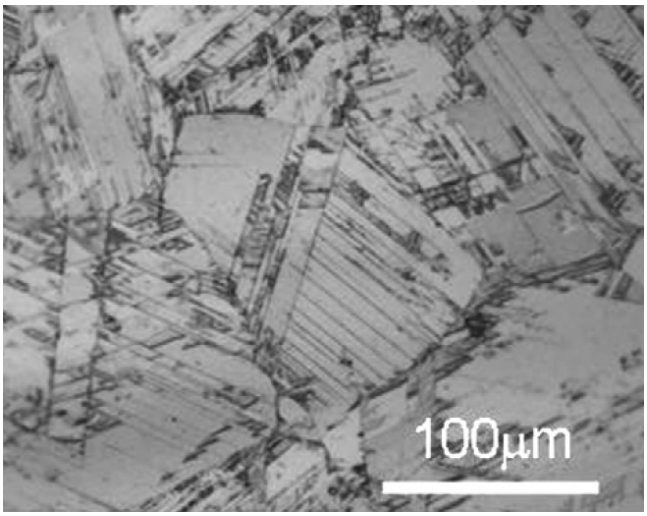

Fig. 1. ε-martensite plates in an Fe-17Mn-6Si-0.3C steel.[8] Reproduced with permission from reference.[8]

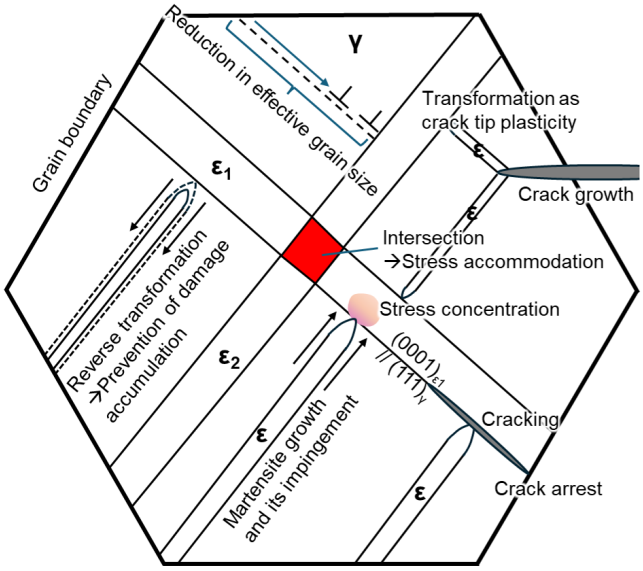

Fig. 2. Schematic illustration of local mechanical phenomena arising from ε-martensite formation. (Online version in color.)

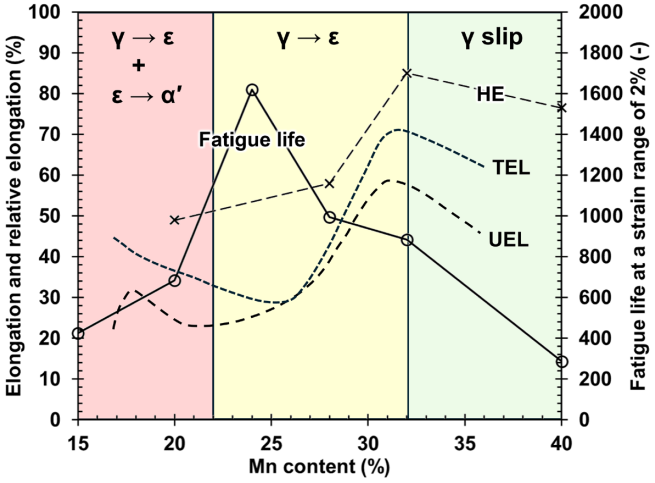

Fig. 3. Tensile property,[11] low-cycle fatigue life,[12] and hydrogen embrittlement (HE) resistance[14] of binary Fe–Mn alloys. HE resistance was measured by tensile testing under hydrogen charging at 10 A/m^2 in a 3%NaCl aqueous solution and was defined as elongation with hydrogen divided by elongation in air, *i.e.*, relative elongation. The composition dependence of the plasticity mechanism was estimated from previous studies.[13,14] TEL: Total Elongation. UEL: Uniform Elongation. (Online version in color.)

transformations in enhancing work hardening capability, the application of γ-ε martensitic transformation remains limited. One key limitation arises from the occurrence of ε-martensite-driven damage formation, which is primarily attributed to the aforementioned first and third hardening mechanisms. In particular, the plastic anisotropy effect, as the third factor, is understood in terms of the crystallographic orientation relationship between the γ-matrix and ε-martensite, specifically the Shoji–Nishiyama orientation relationship.[10] The specific orientation relationship is as follows:

$$(111)_\gamma \,//\, (0002)_\varepsilon\,,\ [\bar{1}10]_\gamma \,//\, [\bar{1}2\bar{1}0]_\varepsilon\,. \quad \ldots\ldots\ldots (1)$$

Therefore, the slip transfer from γ-matrix to ε-martensite on three $\{111\}_\gamma$ planes other than the $(111)_\gamma$ plane requires non-basal shear in ε-martensite, resulting in stress concentration at the γ/ε interface as schematically shown in **Fig. 2**. The stress concentration induces the micro-damage such as crack and void, subsequently causing quasi-cleavage or intergranular fractures. The ε-martensite-driven damage evolution is particularly problematic in high-Mn steels with low stacking fault energy (SFE). Since ε-martensite nucleation originates from intrinsic stacking faults, numerous ε-martensite plates form in high-Mn steels with low SFE at room temperature. Consequently, plasticity-related mechanical properties of high-Mn steels, such as tensile ductility, fatigue life, and hydrogen embrittlement susceptibility, are strongly influenced by γ-ε martensitic transformation behavior and the mechanical characteristics of the resulting ε-martensite.

Figure 3 illustrates the mechanical properties with different Mn contents in Fe–Mn binary alloys, as an example of the mechanical change of steels containing ε-martensite.[11–14] When the Mn content decreases slightly below the critical level for γ-ε martensitic transformation (approximately 32% Mn), uniform elongation improves by approximately 70%, primarily due to the TRIP effect. However, further promotion of γ-ε martensitic transformation, achieved by reducing Mn content from 31% to 20%, accelerates ε-martensite-driven damage evolution, leading to a decline in uniform elongation. Additionally, the difference between uniform and total elongations diminishes as Mn content decreases to 25%, indicating that fracture occurs either immediately after necking initiation or in the absence of necking. Fracture without necking has been linked to quasi-cleavage cracking along ε-martensite plates, as schematically shown in Fig. 2. A further reduction in Mn content allows ε-α' martensitic transformation, which accommodates local stress associated with γ-slip–ε-martensite or ε-martensite–ε-martensite interactions. This stress accommodation effectively suppresses ε-martensite-driven damage evolution, thereby restoring ductility. While hydrogen embrittlement resistance exhibits a similar trend with respect to Mn content, it deteriorates significantly when α'-martensite forms, contrasting with the elongation trend in air.

In the context of low-cycle fatigue, the dependence of fatigue life on Mn content differs markedly from other mechanical properties. Fatigue life reaches its maximum at the Mn content where γ-ε martensite formation is abundant, without transformation of ε-martensite to α'-martensite. This behavior is attributed to γ-ε martensitic transformation at fatigue crack tips[15,16] and the deformation-induced reverse transformation of ε-martensite,[17–19] both of which are introduced later. Hence, to optimize behavior of γ-ε martensitic transformation for enhancing specific mechanical properties, it is essential to comprehensively understand the factors contributing to micro-plasticity-related stress and damage evolution. However, factors causing the ε-martensite-related damage evolution are diverse and multi-scale, particularly in ternary or more complex multi-component alloys, and they act synergistically until final failure. Thus, ε-martensite-driven damage evolution in high-Mn steels remains incompletely understood.

This review aimed to summarize ε-martensite-related damage evolution behavior and mechanisms, focusing on the characteristics of γ-ε martensitic transformation as a plasticity mechanism. Specifically, the damage evolution characteristics associated with tensile ductility, metal fatigue, and hydrogen embrittlement are discussed. Furthermore, potential strategies for leveraging γ-ε martensitic transformation positively, in terms of lattice parameter and phase stability, are briefly introduced.

2. Crystallographic Effect on Plastic Anisotropy: Effects of Phase Stability and Lattice Parameter

As discussed in Section 1, the nucleation of ε-martensite is associated with intrinsic stacking faults or a related fault group. Specifically, when intrinsic stacking faults accumulate on every alternate $\{111\}_\gamma$ plane, the resulting structure becomes HCP, *i.e.*, ε-martensite. Due to the difficulty of non-basal slip, activation of γ-ε martensitic transformation on multiple $\{111\}_\gamma$ planes leads to microscopic stress concentration, microstructural cracking, and macroscopic work hardening. Microscopic stress concentration occurs at boundaries that impede the growth of ε-martensite,[13,20] at the intersections of ε-martensite with twin boundaries,[21] and at intersections of ε-martensite plates.[9] These stress concentrations result in quasi-cleavage and intergranular fractures, as illustrated in **Fig. 4**.[21]

To prevent brittle or brittle-like fracture, concentrated stress at the ε-martensite must be accommodated through optimal intersection mechanisms. Generally, stress induced by local slip is accommodated by further dislocation motion, cross-slip, and dislocation multiplication. However, when the predominant plasticity mechanism is γ-ε martensitic transformation, yielding and subsequent plastic flow are primarily governed by the motion of a/6<211>{111} Shockley leading partials with high Schmid factors (**Figs. 5**(a), 5(b)). Since γ-ε martensitic transformation does not permit the shrinkage of extended dislocations, cross-slip and further atomic shear at the same location on the same slip plane are crystallographically prohibited (Fig. 5(c)).[22] Regarding the local plastic accommodation capability, pop-in behavior observed in nanoindentation experiments demonstrated an interesting result.[23] Figure 5(d) presents an example of load-penetration depth curves of an Fe-28Mn-5Cr-6Si steel, a shape memory alloy.[24] This steel exhibits a significantly lower critical stress for γ-ε martensitic transformation compared to the critical stress for dislocation slip. As a result, the yield stress at room temperature is primarily governed by transformation-induced shear, and the transformation-controlled yield stress is low. Consequently, a low pop-in load, which signifies plasticity nucleation, appears to be low, as shown in Fig. 5(d). Under these conditions, the excursion depth, corresponding to magnitudes of subsequent dislocation motion and multiplication, is small due to the prohibition of dislocation shrinkage (*i.e.*, the transformation dislocations cannot undergo cross-slip or dislocation multiplication). To clarify, the relationship between pop-in load and excursion depth for various steels is shown in Fig. 5(e). The excursion depth generally increases with an increasing pop-in load, because the higher external mechanical driving force leads to a greater amount of dislocation motion after the initiation of plasticity. In this context, a large slope in the relationship between pop-in load and excursion depth indicates a higher required energy per shear displacement by dislocation motion. Thus, the large slope for the Fe-28Mn-5Cr-6Si steel implies that the plastic accommodation capability under identical external energy is more restricted when plasticity is dominated by γ-ε martensitic transformation.

Due to the poor stress accommodation capability in ε-martensite, the γ/ε interfaces and grain boundaries that intercept ε-martensite growth act as preferential sites for local stress evolution. Consequently, a stress accommodation mechanism involving non-basal shear is important to prevent brittle fracture. Particularly, when two ε-martensite plates with different variants intercept or intersect each other, the risk of local stress evolution and subsequent cracking is maximized. Thus, understanding the intersection mechanisms of ε-martensite/slip as well as ε-martensite/ε-martensite is essential for designing structural austenitic steels with high HCP phase stability. As a representative intersection mechanism, the ε-α' martensitic transformation has been observed in austenitic stainless steels[25,26] and high-Mn steels,[6,27] where it effec-

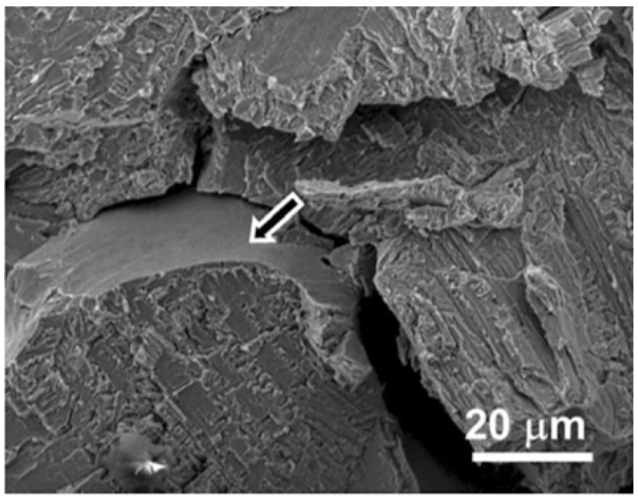

Fig. 4. Example of a fracture surface of a tensile-tested Fe-17Mn-0.3C steel.[21] The arrow indicates a portion of intergranular fracture. Reproduced with permission from reference.[21]

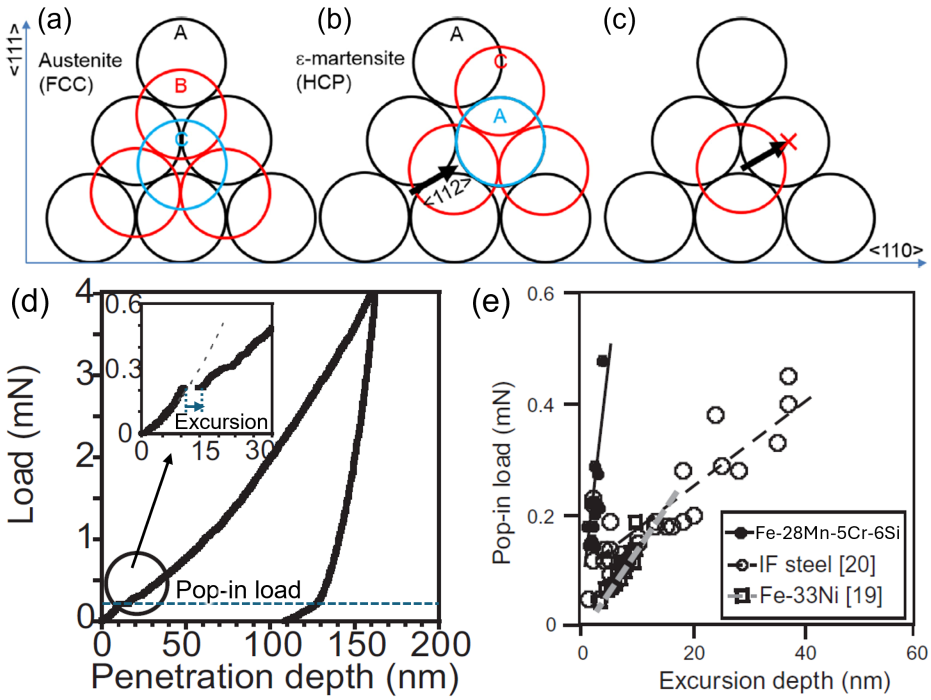

Fig. 5. (a) Atomic arrangement of FCC structure, (b) formation of HCP structure through a/6<112> shear, and (c) restriction of atom movement to the reverse twinning shear direction.[22] (d) Example of load-penetration depth curve obtained by nanoindentation in an Fe-28Mn-5Cr-6Si alloy. (e) Relationship between pop-in load and excursion depth.[23] The inset in (d) shows a magnified view of the highlighted region. Reproduced with permission from references.[22,23] (Online version in color.)

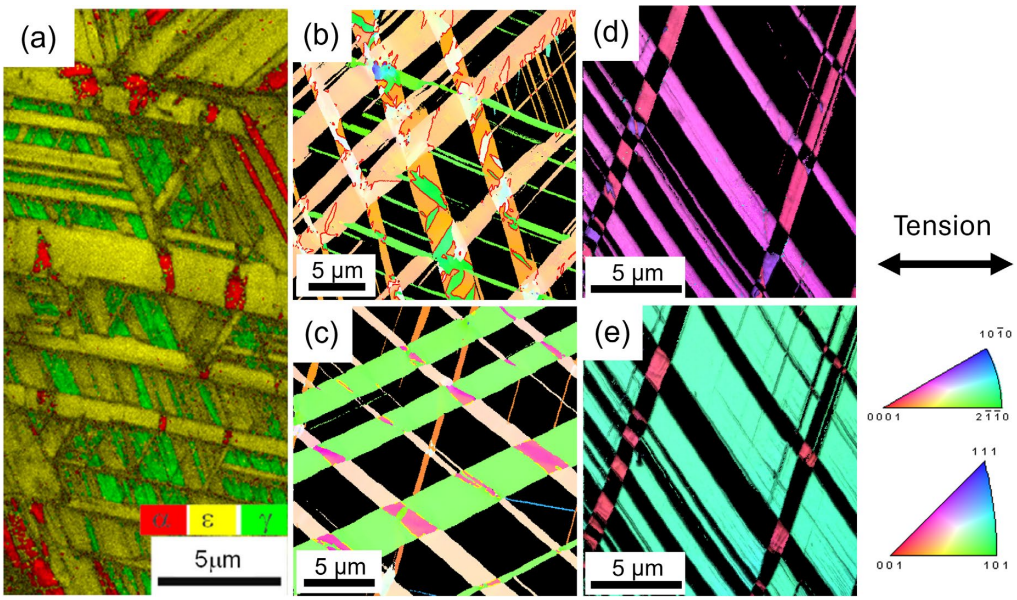

Fig. 6. Intersection microstructures of ε-martensite plates. (a) Phase map showing BCC formation in the Fe-20Mn alloy.[14] Tensile direction IPF maps with boundary identification of (b) {10$\bar{1}$2} and (c) {10$\bar{1}$1} twins. The red lines in (b) and yellow lines in (c) indicate the {10$\bar{1}$2} and {10$\bar{1}$1} twin boundaries, respectively. (d) HCP and (e) FCC tensile direction IPF maps with image quality data, which show the FCC phase at the intersections. Panel (a) was reproduced with permission from reference.[14] The IPF maps in (b–e) are re-analyzed and cropped images from previously published data.[36,39] (Online version in color.)

tively reduces elastic strain energy.[28] **Figure 6**(a) shows an example of ε-α′ martensitic transformation. The BCC transformation from the FCC phase is achieved by the reaction of $a_\gamma/6$<211> twinning shears on different {111} planes.[29,30] For instance, Bogers and Burgers proposed that γ-α′ martensitic transformation can occur via one-third and half twinning shears; they further suggested that the one-third and half twinning shears may result from restructuring of $a_\gamma/6$<211> Shockley partials across multiple parallel {111} planes. Because ε-martensitic transformation occurs via the motion of $a_\gamma/6$<211> Shockley partials on every other {111} plane, ε-martensite intersections or the ε-martensite plate intercepting extended dislocation slips naturally show ε-α′ martensitic transformation when the

free energy of BCC is lower than that of the HCP phase with a low SFE of the austenitic matrix.[31] Furthermore, an elastic strain energy stored within and around the BCC phase at intersections of ε-martensite plates can be accommodated by plastic deformation in the plastically isotropic BCC phase.[31] Therefore, the ε-α' martensitic transformation is an ideal intersection mechanism particularly when the formed α'-martensite is soft. However, the formation of α'-martensite has three disadvantages: (1) cracking at α'-martensite when it is hard, (2) an increase in hydrogen embrittlement susceptibility,[14,32] and (3) deterioration of strain reversibility during cyclic deformation associated with $\gamma \leftrightarrow \varepsilon$ martensitic transformation.[19,33] The detailed mechanisms of the disadvantageous roles of α'-martensite in hydrogen embrittlement and cyclic loading are introduced in subsequent sections.

When the free energy of the HCP phase is sufficiently lower than that of the BCC phase, the stress at the ε-martensite intersections is typically accommodated by $\{10\bar{1}2\}$ and $\{10\bar{1}1\}$ HCP twinning.[34–37] The intersection reactions depend on the crossing shear systems.[36] When the tensile direction of austenite grains is oriented near the [001]-[101] boundary within the [001]-[101]-[111] standard stereographic triangle, the intersection reaction forms $\{10\bar{1}2\}$ twins, as shown in Fig. 6(b). On the other hand, within austenite grains oriented close to the [001]-[111] boundary, the intersection of ε-martensite plates results in $\{10\bar{1}1\}$ twinning, as shown in Fig. 6(c). HCP twinning plays a critical role in stress accommodation at the intersections of ε-martensite plates. However, once HCP twinning occurs, further stress accommodation within the twinned region becomes difficult because the intersection remains plastically anisotropic HCP structure. Therefore, HCP twinning serves as an important stress accommodation mechanism when low strain level is important in applications. For example, in Fe–Mn–Si shape memory alloys, the typical strain provided is generally in the range of 2–8%, and the stored elastic strain energy, along with the remaining HCP structure, is crucial for achieving significant shape recovery strain.

A promising intersection mechanism for large plastic deformation is the formation of the FCC phase, as shown in Figs. 6(d) and 6(e). The FCC phase in intersections of ε-martensite plates is not a twin but is 90°-rotated from the matrix. During the growth of deformation-induced ε-martensite, the stress concentration associated with the shape change of martensite can be accommodated through the $\varepsilon \rightarrow \gamma$ reverse transformation.[38] Similarly, when the free

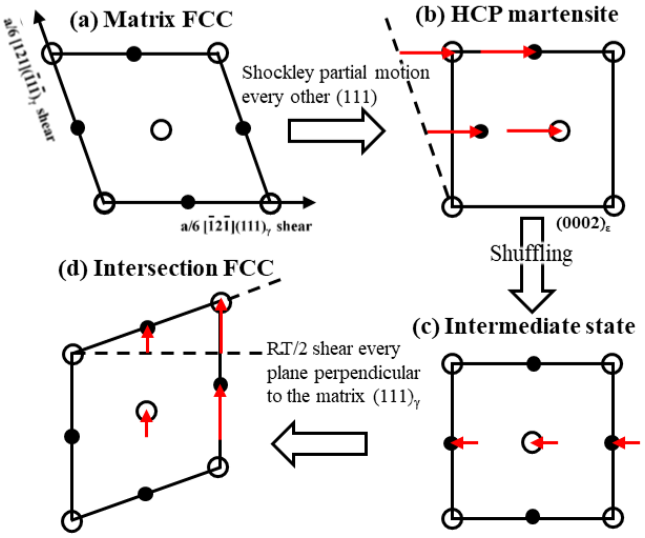

Fig. 7. Schematics for FCC formation at ε-martensite intersections: (a) initial FCC structure, (b) HCP formation via motion of a Shockley partial, (c) half twinning shear that results in an intermediate state, and (d) reverse twinning shear that forms an FCC structure having the orientation observed in Fig. 6(e).[39] RT/2: Half reverse twinning shear. These schematics are modified versions of a previous study.[39] (Online version in color.)

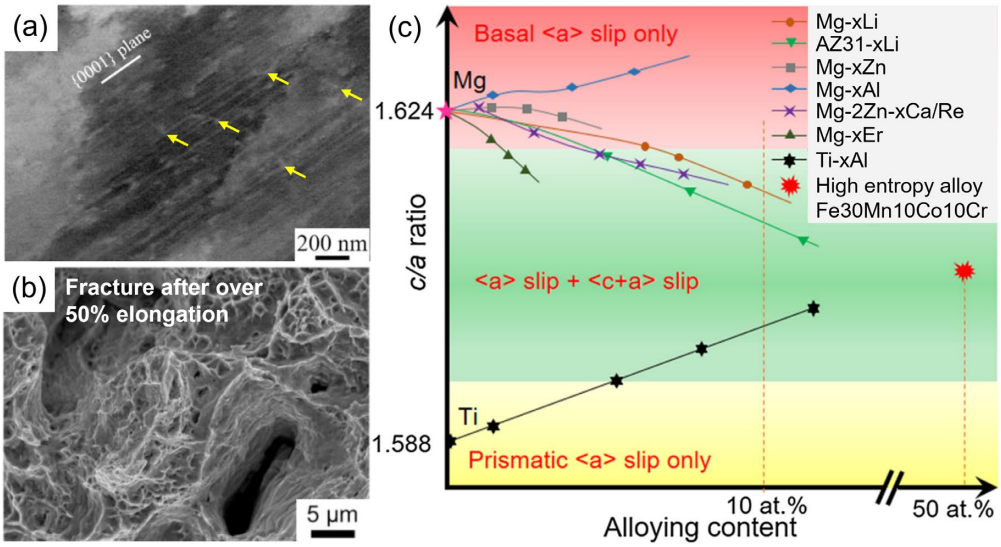

Fig. 8. Characteristics of a ductile Fe-30Mn-10Cr-10Co HEA (at.%) that shows numerous ε-martensite. (a) Electron channeling contrast (ECC) image showing dislocations on non-basal slip plane. The {0001} basal plane is aligned on a nearly edge-on condition, and the dislocations indicated by the yellow arrows are not parallel to the basal plane trace on the surface, indicating that the dislocations are on non-basal planes.[43] (b) Fractograph showing fully ductile feature.[44] (c) *c*/*a* ratio effect on the non-basal slip in various HCP alloys including the HEA[42] Reproduced with permission from references.[42–44] (Online version in color.)

energy of the HCP phase is lower than that of the FCC phase, but the difference between the free energies is small, the formation of the FCC phase is activated at the intersections of ε-martensite plates.[39,40] In terms of crystallography, the FCC phase can form at ε-martensite intersections via the atomic shear shown in **Fig. 7**.[39] This process is based on the shortest path considered in hard sphere models.[30,34,41] Figure 7 shows atomistic arrangements of (a) γ-austenite and (b) ε-martensite viewed from $[101]_\gamma//[1210]_\varepsilon$. All the changes in atomic arrangement in this intersection model occur on this plane. After primary ε-martensite forms via Schockley partial motion every other (111) plane (Fig. 7(b)), impingement of secondary ε-martensite causes local stress evolution. The local stress is accommodated via the shuffling of atoms (Fig. 7(c)) and subsequent reverse half twinning shear on a plane perpendicular to $[101]_\gamma//[1210]_\varepsilon$ (Fig. 7(d)). The structure of Fig. 7(d) is an FCC structure, crystallographic orientation of which is rotated by 90° from the matrix. This corresponds to the crystallographic orientation relationship between matrix and intersection FCC structures shown in the IPF map of Fig. 6(e). The FCC structure in ε-martensite intersections can occur only in thermodynamically and crystallographically restricted conditions as mentioned here. However, the FCC phase is generally soft, tough, plastically isotropic, and resistant to hydrogen embrittlement. Therefore, if the FCC formation can be designed as the primary intersection mechanism, it can act as an ideal stress accommodation mechanism.

The simplest solution for stress accommodation, apart from transformation and twinning, is an increase in non-basal slip activity. Fe-30Mn-10Cr-10Co steel (at.%), which is known as a high-entropy alloy (HEA), exhibits a superior balance between strength and elongation with significant non-basal slip activity[42,43] (**Fig. 8**(a)), demonstrating a fully ductile fracture[44] (Fig. 8(b)) at ambient temperature, despite the occurrence of numerous thermally-induced and deformation-induced γ-ε martensitic transformations.[45,46] The activation of non-basal slip has been explained in terms of the *c/a* ratio of the HCP structure, as illustrated in Fig. 8(c). According to this figure, both <a> basal slip and <c+a> non-basal slip can occur when the *c/a* ratio is approximately 1.61–1.62. While the underlying mechanism of the *c/a* ratio effect requires further investigation, it can serve as a useful indicator for alloy design aimed at activating non-basal slip in ε-martensite. The influence of chemical composition on the *c/a* ratio in Fe–Mn alloys will be discussed in Section 6.2.

3. Damage Evolution during Monotonic Tension

3.1. Cracking Site

In Section 2, we introduced the importance of stress accommodation, along with its solution based on plasticity mechanisms at the ε-martensite plates. However, when the selectable composition is restricted to obtaining high cost-performance and other properties such as the shape memory effect, the ε-martensite-driven damage evolution may become unavoidable. In this case, we must understand the underlying mechanism of the damage evolution stemming from interactions of ε-martensite and microstructural boundaries. In this section, we introduce the ε-martensite-driven damage initiation mechanism during monotonic tensile deformation. The representative damage mechanism is transgranular cracking associated with stress concentration at ε-martensite tips impinged at a preexisting thick ε-martensite plate. Considering that deformation-induced γ-ε martensitic transformation is intercepted at an interface between matrix and preexisting ε-martensite, as shown in

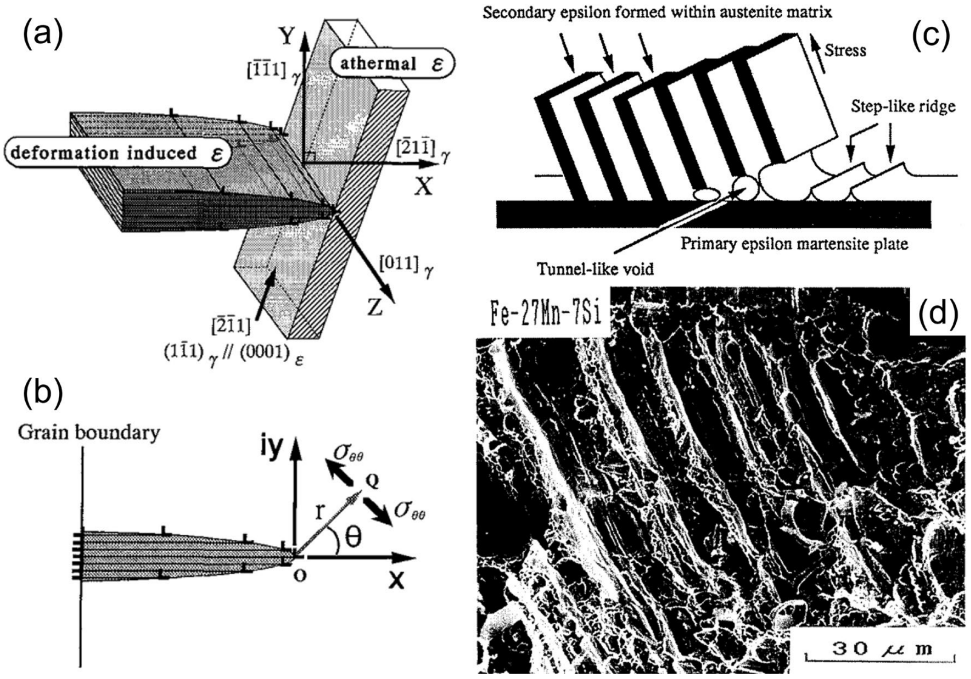

Fig. 9. (a) Schematic for the crystallography of ε-martensite impinged at pre-existing ε-martensite. (b) Micromechanical stress description at an ε-martensite plate tip.[20] (c) A schematic for the fracture mechanism along ε-martensite plates and (d) quasi-cleavage fracture in an Fe-27Mn-7Si alloy.[48] Reproduced with CC license from references.[20,48]

Fig. 9(a), the leading partial dislocations at the ε-martensite tip on every other {111} plane experience a repulsive force. Therefore, the local stress arising from the repulsive stress can be estimated using the dislocation pile-up model.[47] Assuming the coordinate, martensite morphology, and martensite alignment shown in Fig. 9(b), the normal stress on the OQ plane around the ε-martensite tip $\sigma_{\theta\theta}$ can be estimated by the following equation:[20]

$$\sigma_{\theta\theta} = \frac{3}{2}\left(\frac{4n}{r}\right)^{1/2} \sigma_0 \sin\theta\cos\frac{\theta}{2}, \quad \cdots\cdots\cdots\cdots (2)$$

where n is the number of piling-up partial dislocations, σ_0 is the stress required for the motion of leading partials. According to Eq. (2), $\sigma_{\theta\theta}$ is maximized at θ = 70.5°. As the angle between the two {111} planes along the growing ε-martensite and preexisting ε-martensite is 70.32°, the concentrated tensile stress at the deformation-induced ε-martensite tip effectively acts as a driving force for cracking at the matrix/preexisting ε-martensite interface. When stress accommodation at the ε-martensite intersection is insufficient, a crack or void can form, as illustrated in the schematic in Fig. 9(c).[48] The tunnel-like damage void, followed by coalescence along the preexisting ε-martensite plate, leads to quasi-cleavage fracture and the formation of step-like ridges on the fracture surface, as shown in Fig. 9(d). This damage formation mechanism occurs predominantly when the preexisting ε-martensite formed during water quenching, as thermally-induced ε-martensite is typically thick.[20]

Another preferential plane for the ε-martensite-driven damage is the Σ3 twin boundary. An Fe-17Mn-0.3C steel exhibits poor ductility at ambient temperature, as shown in **Fig. 10**[1], which is attributed to quasi-cleavage fracture along the {111} plane (the major portion of Fig. 4(b)). The cracked {111} plane does not align with ε-martensite plates but follows the annealing twin boundaries (**Figs. 11**(a), 11(b)).[52] Therefore, the interaction between ε-martensite and the twin boundary results in a brittle-like fracture.

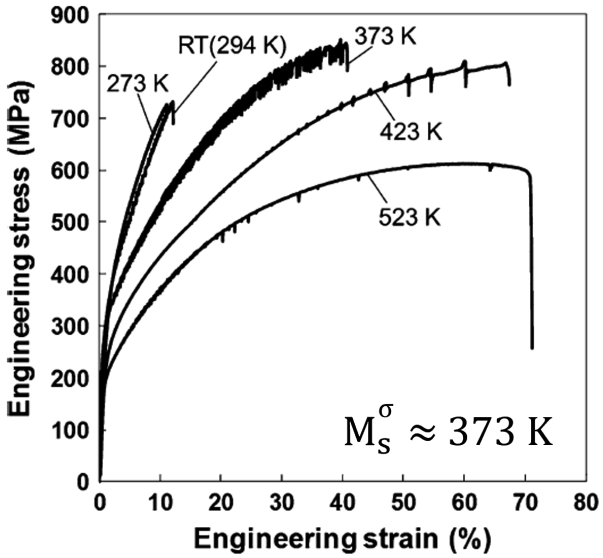

Fig. 10. Engineering stress-strain curves with different deformation temperatures in an Fe-17Mn-0.3C steel.[21] Reproduced with permission from reference.[21]

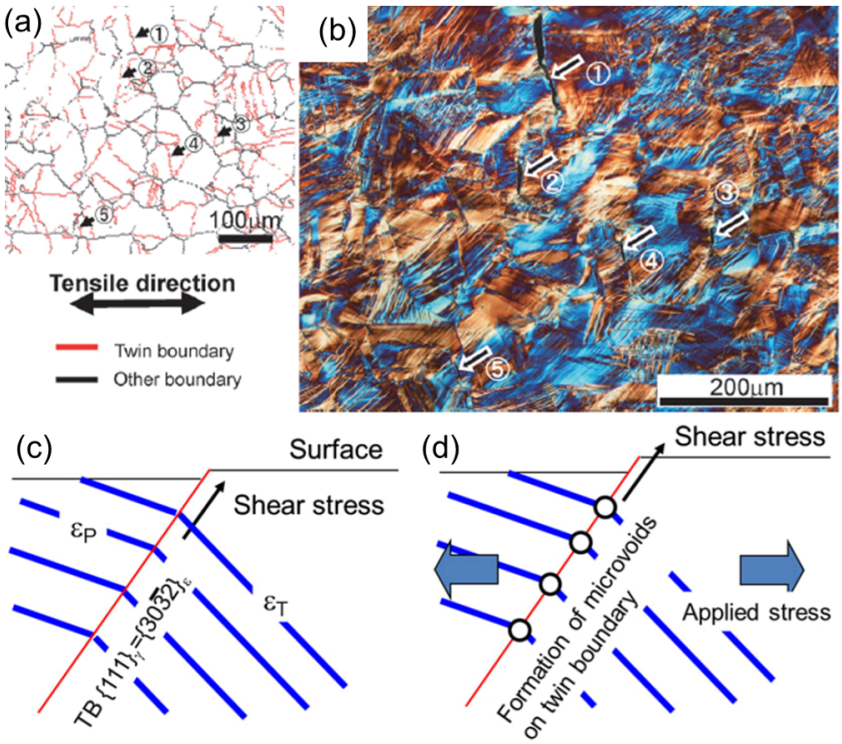

Fig. 11. (a) Boundary map and (b) optical image showing Σ3 twin boundary cracking in the Fe-17Mn-0.3C steel deformed at room temperature.[52] The numbers with arrows in (a) and (b) indicate identical locations. (c, d) Schematics for possible cracking mechanism associated with interactions of ε-martensite and twin boundary.[21] Reproduced with permission from references.[21,52] (Online version in color.)

[1] The serrated flow on the stress-strain curves is attributed to carbon-driven dynamic strain aging.[49–51]

Because the crystallographic plane of FCC twin boundaries is also {111}, the stress concentration at the ε-martensite tip effectively acts as a factor causing the twin boundary cracking. However, the crystallographic structure beyond the twin boundary is also FCC, in contrast to the matrix/ε-martensite interface. Therefore, the leading partials of growing ε-martensite can relatively easily penetrate the twin boundary through dislocation dissociation reactions such as twin-twin interactions,[53,54] which accommodate stress at the twin boundary. A significant issue occurs after ε-martensite penetrates the twin boundary. When $a/6[\bar{1}12](\bar{1}1\bar{1})$ leading partials penetrate a $(\bar{1}11)$ twin boundary, where a is the lattice parameter of austenite, the following dislocation dissociation reaction occurs:[53]

$$3\times a/6\left[\bar{1}12\right]\left(\bar{1}1\bar{1}\right)\rightarrow 3\times a/18\left[\bar{5}52\right]\left(11\bar{5}\right) +2\times a/6\left[1\bar{1}2\right]\left(\bar{1}11\right). \quad \text{..... (3)}$$

$a/18[\bar{5}52](11\bar{5})$ is equal to a/6[112] in the twin. Equation (3) indicates that a partial dislocation slip on the crossed twin boundary is required for the twinning shear transfer. Thus, after the penetration of the first group of leading partials, subsequent partial dislocation motion across the twin boundary requires non-basal shear in the ε-martensite consisting of the first group of leading partials (Fig. 11(c)). In the case of Fe-17Mn-0.3C steel, non-basal slip is restricted, and carbon-bearing "hard" α'-martensite forms instead of non-basal slip. Therefore, the intersections of ε-martensite and twin boundary act as preferential sites for stress evolution and subsequent damage initiation (Fig. 11(d)). Hence, when the normal of the twin boundary is aligned to the near-tensile direction,[21] the damaged twin boundaries show brittle-like fracture.

Even when the intersection problems are solved, grain boundary impinging ε-martensite also acts as a damage initiation site when the plastic strain becomes large.[55,56] For example, as shown in **Fig. 12**(a), a portion of a grain boundary intercepting ε-martensite shows a significant contrast change in the ECC image, indicating stress concentration. The stress concentration causes nano-cracks/voids along grain boundaries (Fig. 12(b)). The micro-damage grows through plastic deformation and coalescence of multiple cracks/voids. Furthermore, nano-cracks/voids newly form near tips of growing damages (Fig. 12(c)), which accelerates the damage growth along grain boundaries. Coalescence of the multi-scale size damage yields long cracks, which significantly contributes to final failure. The process is schematically drawn in Figs. 12(d)–12(f). Hence, improvement of stress accommodation capability can delay the damage initiation and growth, but complete suppression of ε-martensite-driven damage initiation is difficult because of the various patterns of ε-martensite/boundary interactions as long as γ-ε martensitic transformation is used as the primary plasticity mechanism. In this context, it is also crucial to consider strategies to prevent damage growth, which are discussed in the following section.

3.2. Crack Arrest

After examining the damage initiation and fracture mechanisms, two solutions can be proposed to improve the ductility of ε-martensite. The first solution involves avoiding stress concentration at potential damage initiation sites, which can be achieved by controlling the stress accommodation mechanisms discussed in Section 2. Alternatively, even

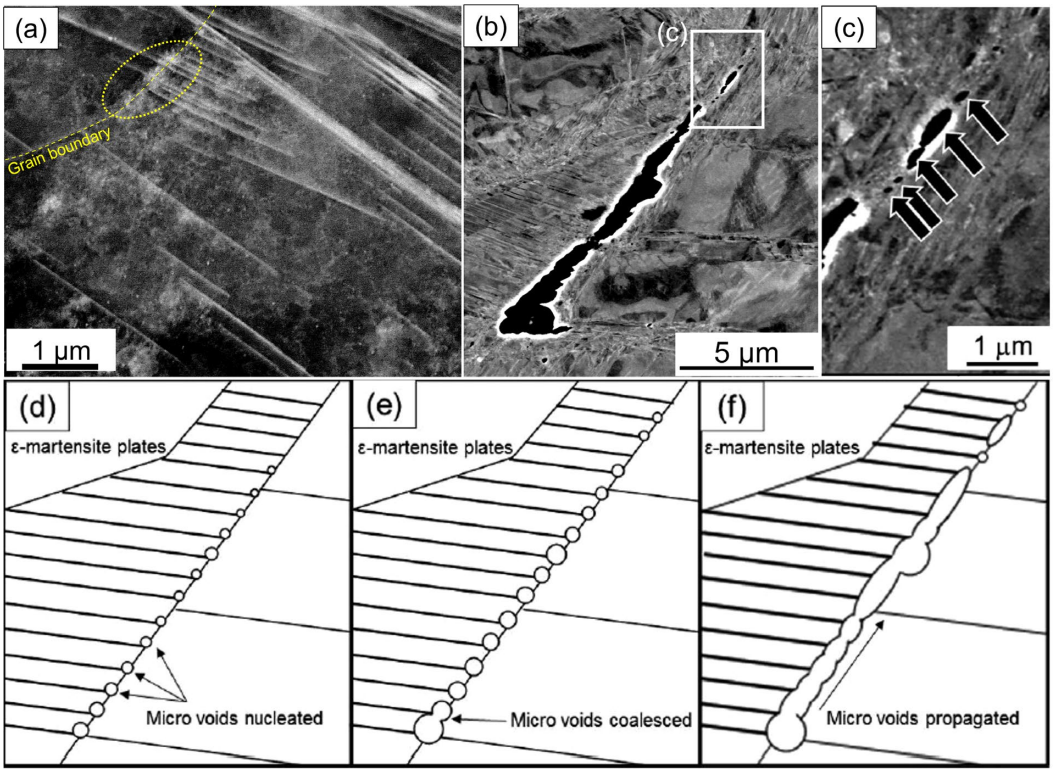

Fig. 12. ECC images showing (a) grain boundary intercepting ε-martensite plates, (b) damage initiation and growth, and (c) its magnification in an Fe-28Mn alloy. (d–f) Schematics for the damage evolution along the grain boundary.[55,56] Reproduced with permission from reference.[55] (Online version in color.)

when damage initiation is inevitable, the microstructural crack arrestability can be improved. An example of damage evolution, from initiation to final failure, is introduced here using Fe-28Mn alloy that undergoes deformation-induced γ-ε martensitic transformation. **Figure 13**(a) presents the stress-strain curve of the solution-treated Fe-28Mn alloy at ambient temperature. The alloy exhibits micrometer-scale damage initiation even during the uniform deformation stage (Fig. 13(b)), but the damage size does not increase significantly with further deformation until a certain level of strain is reached. The variations in damage size and aspect ratio with strain are summarized in Figs. 13(c) and 13(d). The damage lengths, a and b, used to define the damage aspect ratio are shown schematically in Figs. 13(b_1) and 13(b_2). All the damage data were obtained from the fractured hour-glass-shaped specimen and were plotted against local plastic strain. Here, damage is defined as sub-micrometer to micrometer-scale cracks/voids detectable by optical microscopy[57] and scanning electron microscopy.[58–60] Further details of the damage quantification method have been reviewed elsewhere.[61] Through quantitative damage analysis, the damage evolution behavior was classified into three regimes: (i) the damage incubation regime (where a precursor of damage evolves with strain), (ii) the damage nucleation regime (where damage forms but does not undergo significant growth), and (iii) the damage growth regime. In the nucleation regime, damage initiates but its size does not show substantial growth. As seen in Fig. 13(d), the damage aspect ratio increased significantly in this regime, indicating that the propagation of sharp damage, *i.e.*, cracks, was arrested by tip blunting. Due to this microcrack "arrest," the alloy displayed large elongation, despite the occurrence of numerous damages during deformation. Therefore, the relationship between the microstructure and microcrack arrest is key to achieving superior elongation in the presence of ε-martensite.

Figure 14(a) shows a phase map displaying the ε-martensite distribution around a small damage. One side of the damage shows a sharp tip, while the other side exhibits tip blunting. Notably, the sharp crack region (A) contains ε-martensite, whereas the blunt crack tip region (B) contains only austenite. This heterogeneous distribution of ε-martensite arises from the crystallographic orientation dependence of deformation-induced γ-ε martensitic transformation. Specifically, deformation-induced γ-ε martensitic transformation preferentially occurs when the tensile orientation is aligned with <111>, whereas <001>-oriented grains remain as austenite.[62] As schematically illustrated in Fig. 14(b), when a considerable amount of ε-martensite exists at and near the crack tip, crack propagation or new damage initiation and coalescence occur, resulting in a sharp crack tip. On the other hand, when the austenite at and ahead of the crack tip is crystallographically stable, significant crack tip blunting occurs, thereby enabling crack arrest. Because <001>-oriented austenite grains persist even at later stages of tensile deformation,[62] damage arrestability is maintained until damage coalescence occurs in the damage growth regime.

Crack arrestability depends on the fraction, morphology, and ductility of ε-martensite. The characteristics of ε-martensite are sensitive to the chemical composition. In particular, the effects of Si and C distinctly influence the

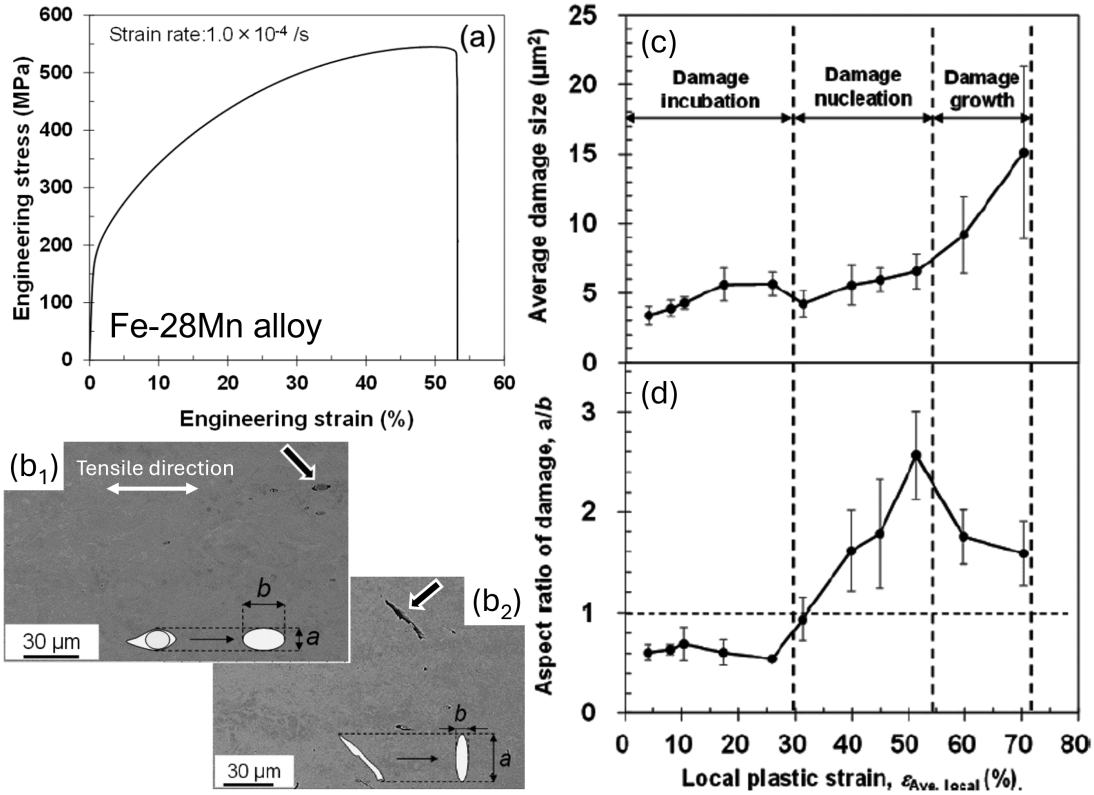

Fig. 13. Tensile behavior and damage evolution in the Fe-28Mn alloy.[55,56] (a) Stress–strain curve. (b_1, b_2) Examples of damage. The insets indicate the definition of the aspect ratio of damage. (c) Average damage size and (d) aspect ratio of damage plotted against local plastic strain. Reproduced with permission from reference.[55]

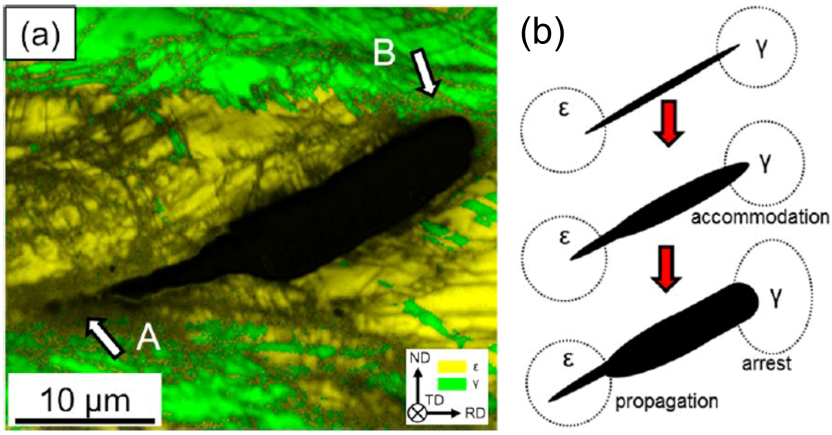

Fig. 14. (a) Microcrack arrest depending on crack tip microstructure in the Fe-28Mn alloy deformed at ambient temperature. (b) A schematic for the microcrack arrest at austenite and growth within ε-martensite.[55,56] Reproduced with permission from reference.[55] (Online version in color.)

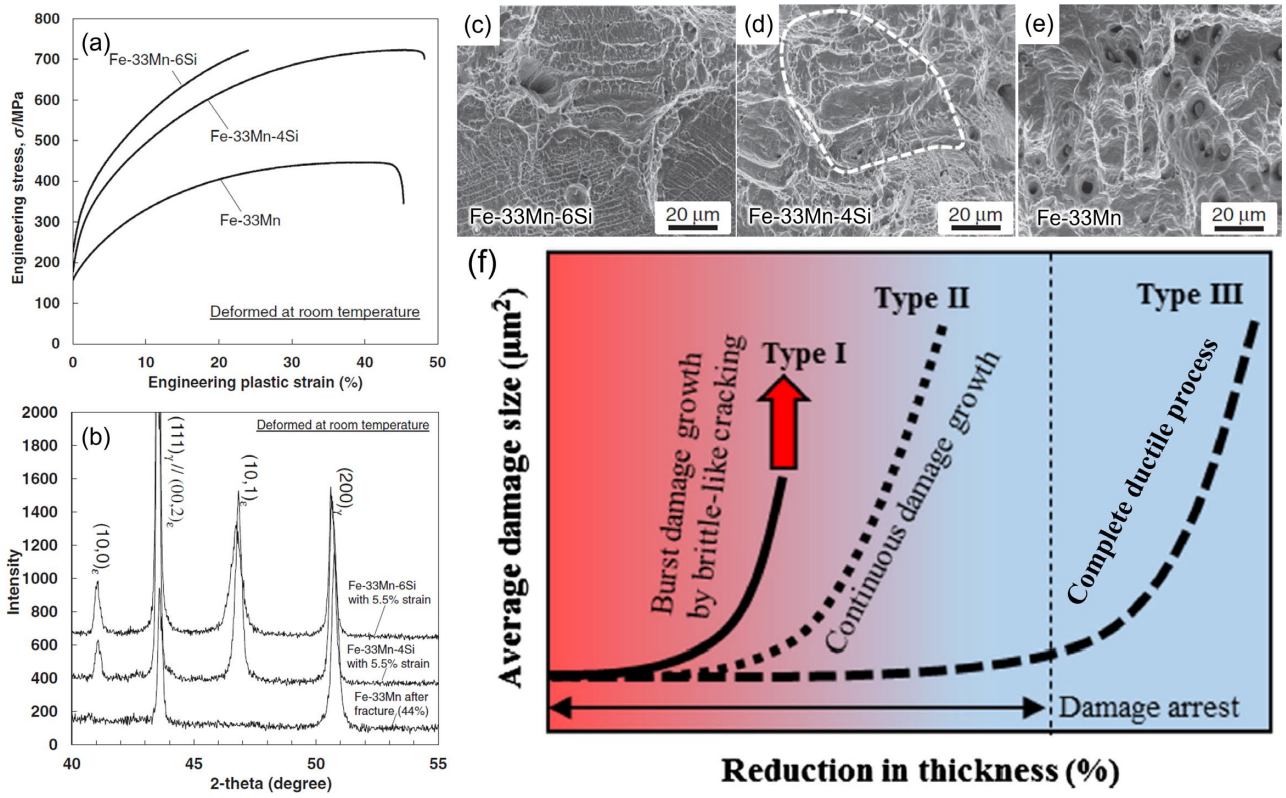

Fig. 15. (a) Stress-strain curves of Fe-33Mn-xSi alloys. (b) The XRD profiles of deformed Fe-Mn-xSi alloys. (c–e) Fractographs obtained by tensile tests at ambient temperature.[66] (f) Classification of ε-martensite-related damage evolution.[67] Reproduced with permission from references.[66,67] (Online version in color.)

ε-martensite characteristics and associated damage evolution behavior, which will be discussed further in Section 6.1. **Figure 15** provides an example of the effect of Si on tensile fracture behavior. The Fe-33Mn-6Si steel is a shape memory alloy that exhibits $\gamma \leftrightarrow \varepsilon$ reversible transformation. The addition of Si generally promotes deformation-induced γ-ε martensitic transformation in high-Mn steels due to a reduction in the SFE[63,64] and solution hardening of the austenite matrix.[8,65] Figures 15(a) and 15(b) demonstrate that deformation-induced γ-ε martensitic transformation leads to high work hardening ability compared with that of the Fe-33Mn binary alloy, in which no γ-ε martensitic transformation occurs even after fracture.[66] However, the Fe-33Mn-6Si steel exhibited low elongation due to premature fracture. Interestingly, the Fe-33Mn-4Si steel exhibited a similar amount of ε-martensite at the same strain as that of the Fe-33Mn-6Si steel, but fracture occurred after necking. Therefore, the strength-ductility balance was maximized in the Fe-33Mn-4Si steel. The reason for the ductile fracture in the presence of ε-martensite can be understood by examining the fracture surface. The fracture surface of the Fe-33Mn-6Si steel displayed quasi-cleavage fracture involving step-like ridges (Fig. 15(c)), which is a characteristic feature of ε-martensite-related fracture. When the Si content was 4%, a similar fractographic feature was observed, as highlighted in Fig. 15(d), but the depth of the step-like ridge was deeper, comparable to the dimple depth observed in the Fe-33Mn binary alloy, except for the inclusion parts (Fig.

15(e)). The deeper ridge formation occurred when the tips of ε-martensite-driven damages were significantly blunted during damage growth. Thus, the fracture surfaces suggest that microcrack arrest occurred in the Fe-33Mn-4Si steel, but not in the Fe-33Mn-6Si steel. Moreover, an extreme case such as room temperature deformation in the Fe-17Mn-0.3C steel shows brittle-like cracking at ε-martensite, resulting in poor ductility (Fig. 10). Based on these findings, the damage evolution behavior can be classified into three types, as schematically shown in Fig. 15(f).[67] Type I is characterized by premature fracture associated with brittle-like quasi-cleavage fracture, in which effective crack arrest does not occur (*e.g.*, the case of Fe-17Mn-0.3C steel and low-temperature embrittlement in high-Mn steels). Type II is characterized by continuous damage growth from the early deformation stage, where crack blunting occurs, but new damage formation and subsequent damage coalescence cannot be avoided. Type III is characterized by microcrack arrest, where crack arrest significantly contributes to macroscopic ductility, as seen in the Fe-33Mn-4Si steel. Therefore, to obtain the beneficial effects of ε-martensite, its fraction must be high, but the boundary strength, stress accommodation capability, and heterogeneous microstructure enabling microcrack arrest must be carefully designed to maximize the strength-ductility balance.

4. Damage Evolution during Cyclic Loading

From a fatigue perspective, γ-ε martensitic transformation plays dual roles in fatigue crack initiation and growth. Tension-induced ε-martensite can reversibly transform under compressive deformation.[12,18,19] This reversible transformation, coupled with the crystallographic constraint of plasticity,[22] prevents damage accumulation and the associated crack growth during cyclic deformation.[15,33,68] Further details regarding the relationship between γ-ε martensitic transformation and fatigue crack resistance have been reviewed elsewhere.[16,69] However, in steels where Type I damage evolution with ε-martensite occurs in tensile fracture, the brittle-like features also degrade its resistance to fatigue crack growth. **Figure 16**(a) presents an example of fatigue crack growth involving deformation-induced γ-ε martensitic transformation. Due to the beneficial effects of γ-ε martensitic transformation, an Fe-30Mn-4Si-2Al steel exhibited excellent fatigue crack growth resistance compared with that of an Fe-30Mn-6Al steel, in which no martensitic transformation occurs. In contrast, the crack growth rates in an Fe-30Mn-6Si steel, exhibiting ε-martensite-driven quasi-cleavage fracture in tensile tests,[70] were higher than those in the Fe-30Mn-4Si-2Al steel. The fatigue fracture surface shown in Fig. 16(b) also displays a quasi-cleavage fracture feature, with longitudinal cracks indicated by the black arrows. This brittle-like feature resulted from discontinuous fatigue cracking along $\{111\}_\gamma//\{0002\}_\varepsilon$ ahead of the main fatigue crack tip (Fig. 16(c)). The initiated subcracks grow (Fig. 16(d)) and coalesce (Fig. 16(e)). This subcrack initiation and coalescence process repeats, leading to rapid crack growth. A significant portion of the brittle-like fatigue crack occurs within the ε-martensite-dominant region and along one of the ε-martensite plate alignments, as shown in **Fig. 17**. Therefore, the ductility of ε-martensite is crucial not only for monotonic tensile deformation but also for cyclic deformation.

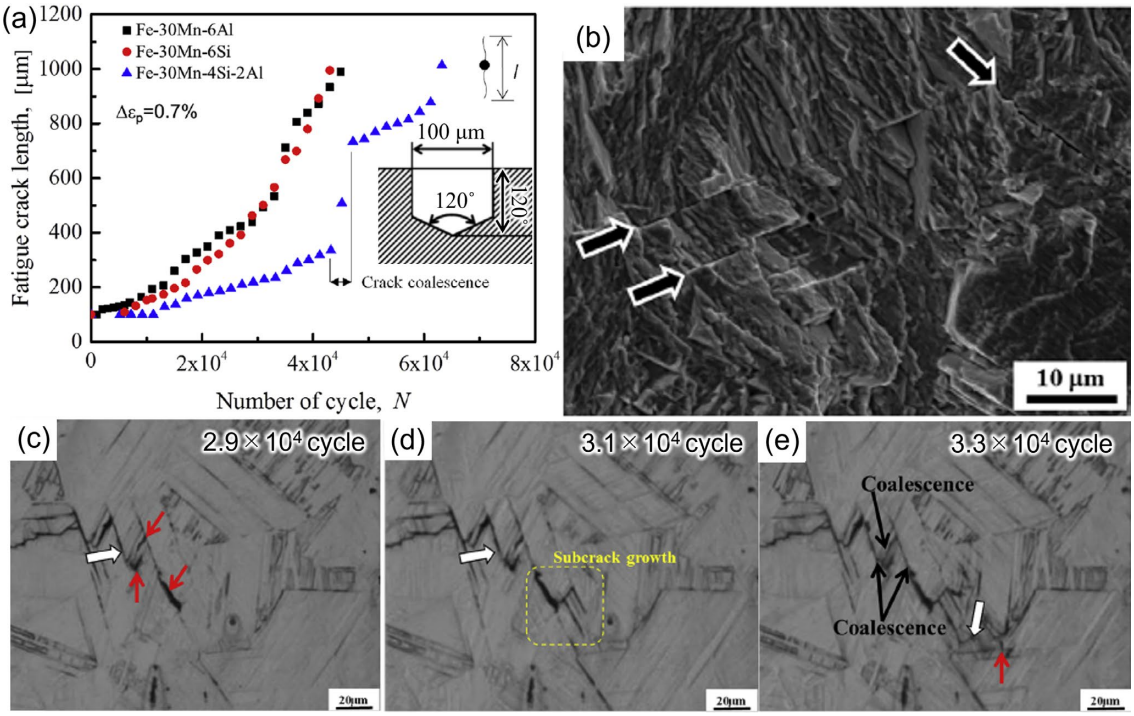

Fig. 16. (a) Crack length plotted against the number of cycles in Fe-30Mn-6Al, Fe-30Mn-6Si, and Fe-30Mn-4Si-2Al alloys, which was obtained by fully reversed bending fatigue test at a total strain range of 0.7% using specimens with a drill hole as a crack starter. The drill hole geometry is shown as the inset. (b) Fracture surface and (c–e) crack propagation process of the Fe-30Mn-6Si alloy.[68] The white and red arrows indicate the main crack tip and subcracks, respectively. Reproduced with permission from reference.[68] (Online version in color.)

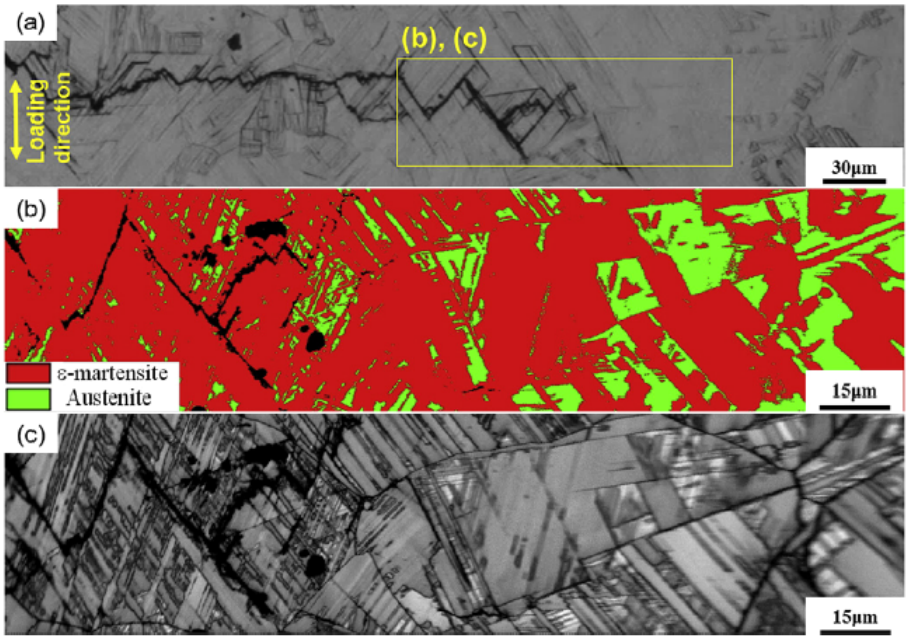

Fig. 17. (a) Optical image, (b) phase map, and (c) IQ map around the fatigue crack tip of the Fe-30Mn-6Si alloy.[68] The test method is the same as Fig. 16. Reproduced with permission from reference.[68] (Online version in color.)

5. Hydrogen Embrittlement

High-Mn steels exhibit hydrogen embrittlement fracture.[71–73] In particular, microstructures containing ε-martensite are vulnerable to hydrogen embrittlement.[74–76] Hydrogen significantly affects cracking resistance as well as γ-ε[77] and ε-α'[78] martensitic transformation behaviors. The effect of hydrogen on γ-ε martensitic transformation has been reviewed in the literature;[79] therefore, this section focuses on the relationship between microstructure and cracking under the influence of hydrogen. **Figure 18**(a) illustrates hydrogen embrittlement susceptibility of binary Fe–Mn alloys evaluated by tensile testing under electrochemical hydrogen charging with different cathodic current densities. The relative elongation, ε_{RE}, was defined as

$$\varepsilon_{RE} = 100 \times \varepsilon_H / \varepsilon_{air}, \quad \text{..... (4)}$$

where ε_H and ε_{air} indicate total elongations obtained from tensile testing with hydrogen and in air, respectively. ε-martensite in the Fe-20Mn binary alloy is metastable against the BCC phase, enabling subsequent transformation to α'-martensite. As schematically shown in Fig. 18(b), the α'-martensite acts as a preferential hydrogen-related cracking site, because the α'-martensite contains a supersaturated amount of hydrogen[78,80] and exhibits high hydrogen diffusivity, which promotes rapid hydrogen localization at stress-concentration sites.[81] Therefore, the Fe-20Mn alloy exhibits the lowest hydrogen embrittlement resistance among the four Fe–Mn binary alloys. When the Mn content increases to 28%, ε-martensite becomes stable. Comparing Fe-20Mn and Fe-28Mn alloys reveals that stable ε-martensite has a smaller impact on hydrogen embrittlement susceptibility. As a general negative effect, γ-ε martensitic transformation induces stress concentration, particularly at the interaction points between growing ε-martensite and obstacle boundaries (*e.g.*, γ/ε interface and grain boundary), which acts as a mechanical driving force for cracking. Hydrogen assists the ε-martensite boundary cracking, which deteriorates crack/void initiation resistance and microcrack arrestability.[82] This disadvantageous effect becomes more pronounced when ε-martensite has a low stress accommodation capability and a high fraction. However, as the Mn content increases and the ε-martensite fraction decreases during deformation, the negative effect is gradually suppressed. Since cracks can propagate easily along ε-martensite plates but not easily across the plates, the γ/ε interface can arrest cracks when the ε-martensite fraction is low, and the plates are aligned perpendicular to the crack propagation direction. Therefore, hydrogen embrittlement resistance increases with increasing Mn content up to 32% in the binary alloy. A further increase in Mn content to 40% completely suppresses γ-ε martensitic transformation and reduces resistance to grain boundary cracking. Consequently, the Fe-32Mn alloy exhibits the highest resistance to hydrogen embrittlement. Thus, the hydrogen embrittlement resistance of binary Fe–Mn alloys is determined by the balance between ε-α' transformability, ε-martensite characteristics, and grain boundary strength. It is also noteworthy that the ε-martensite-related hydrogen embrittlement behavior is dependent on strain rate. Generally, hydrogen embrittlement is recognized to be a time-dependent phenomenon because of competitive interaction of dislocation and hydrogen,[83–85] hydrogen localization to stress concentration sites,[86–89] and hydrogen diffusion/segregation at specific microstructures such as grain boundary.[90,91] In addition to those factors, ε-martensite fraction at a strain increases with decreasing strain rate, and the fraction is further increased by hydrogen charging.[92] The promoted γ-ε martensitic transformation at a low strain rate accelerates hydrogen-assisted failure in tensile tests.

Figure 19(a) presents the hydrogen embrittlement behavior of a Fe-high-Mn alloy with a complex chemical composition, namely, Fe-30Mn-10Cr-10Co HEA (in at.%).[93] The HEA demonstrates large elongation due to the TRIP

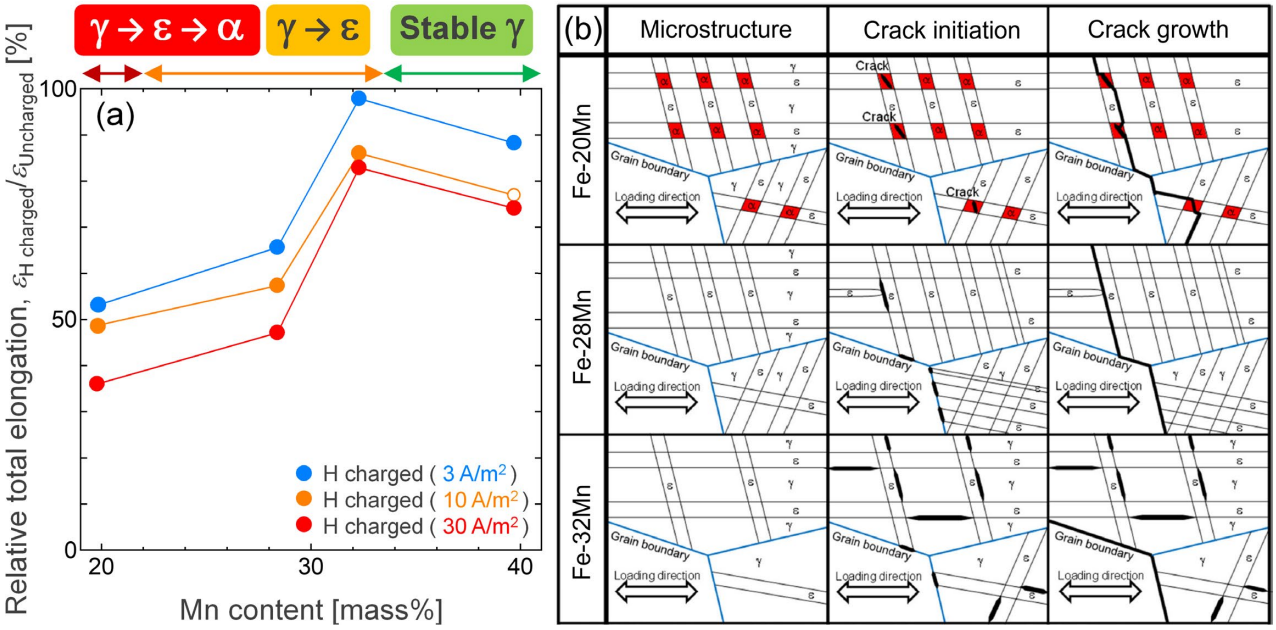

Fig. 18. (a) Mn content dependence of tensile elongation loss evaluated by tensile testing under hydrogen charging in the Fe-20Mn, Fe-28Mn, Fe-32Mn, and Fe-40Mn alloys.[14] The hydrogen charging was performed in a 3%NaCl aqueous solution containing 3g/L NH_4SCN. Reproduced with permission from reference.[14] (b) Schematics for hydrogen embrittlement crack initiation and growth. (Online version in color.)

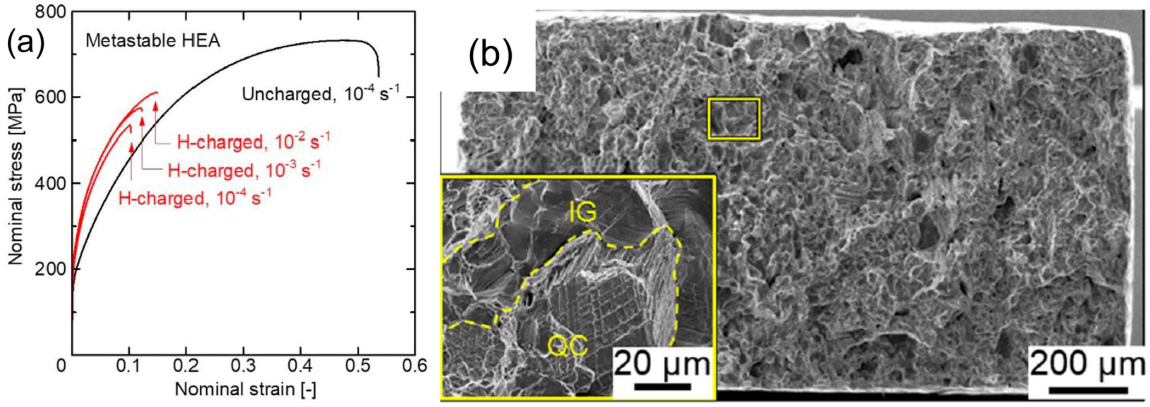

Fig. 19. (a) Stress–strain curves of a Fe-30Mn-10Cr-10Co HEA with and without gaseous hydrogen charging at 100 MPa[93] and (b) the fracture surface of the hydrogen-charged specimen tested at 10^{-4} s^{-1}.[94] Reproduced with permission from references.[93,94] (Online version in color.)

effect associated with γ-ε martensitic transformation. Interestingly, the fracture mode in air is fully ductile, likely owing to the activation of non-basal slip, as previously discussed in Fig. 8. Hydrogen alters the fracture mode to intergranular or quasi-cleavage fractures, as shown in Fig. 19(b).[94] The quasi-cleavage fracture surface, with shallow step-like ridges, resembles the fractographic feature shown in Fig. 15(c), suggesting that the damage evolution type changed from type III to type I. Specifically, hydrogen not only deteriorates damage initiation resistance but also impairs the micrometer-scale crack arrestability along ε-martensite plates. Furthermore, the grain-size-scale crack arrestability, such as that shown in Fig. 14, is also degraded due to intergranular fracture. Consequently, hydrogen significantly reduces the elongation of the HEA. In terms of quasi-cleavage fracture, a critical factor contributing to the ductility of ε-martensite in the HEA is the lattice-parameter-dependent non-basal slip, which could prevent fracture along the ε-martensite plates. In this context, hydrogen, even in small amounts, significantly alters the lattice parameter of ε-martensite,[95] which may disrupt the optimal lattice parameter balance of a and c axes for non-basal slip in the HCP structure.

6. Alloy and Microstructure Design toward a Use of ε-martensite

6.1. Grain Refinement

As discussed previously, the detrimental phenomena causing ε-martensite-related damage are the intersection or interception of ε-martensite plates and the stress concentration resulting from the impingement of ε-martensite growth at grain boundaries. Both of these phenomena can be simultaneously suppressed through grain refinement. In low SFE FCC alloys, grain boundary stress concentration, which arises from the impingement of deformation-induced microstructural evolution (such as planar slip and γ-ε martensitic transformation), is significantly reduced by

increasing the number density of grain boundaries. This reduction suppresses intergranular cracking,[13,96–99] which can be understood based on dislocation pile-up theory.[100–102] Furthermore, grain refinement suppresses thermally induced γ-ε martensitic transformation and constrains the variant selection of ε-martensite to a single variant. This minimizes the occurrence of thick ε-martensite plates and the intersections of ε-martensite plates. **Figure 20** illustrates the effect of grain size on the microstructure, mechanical properties, and fracture behavior of binary Fe–Mn alloys.[13] The Fe-22Mn alloy is most notably affected by quasi-cleavage cracking, which is associated with the interactions between thermally induced and deformation-induced ε-martensite plates in the binary alloys. This is because numerous thermally induced ε-martensite plates form without undergoing ε-α' martensitic transformation, a process that effectively serves as a stress accommodation mechanism (Fig. 20(a)). Grain refinement reduces the ε-martensite fraction (Fig. 20(b)) and constrains variant selection, leading to significant improvements in both the strength and ductility of the Fe-22Mn alloy. This is achieved by decreasing the grain size from 100 to 10 μm (Figs. 20(c), 20(d)). Figure 20(e) provides a schematic representation of the relationship between microstructural changes and fracture behavior in the Fe-22Mn alloy. As grain boundary damage is suppressed by grain refinement, as shown schematically in Fig. 20(f), other binary compositions containing deformation-induced ε-martensite, *e.g.*, Fe-27Mn alloy, also exhibit simultaneous improvements in both strength and elongation. Therefore, the effect of grain refinement is particularly important in suppressing ε-martensite-related damage evolution and the associated brittle-like fracture.

6.2. Lattice Parameter Design

As shown in Fig. 8(c), the lattice parameter of ε-martensite plays a critical role in suppressing ε-martensite-related damage formation in austenitic steels containing HEAs. The effects of specific solute elements on lattice parameters in binary and ternary Fe–Mn alloys have been systematically examined; thus, the composition dependence of lattice parameters is summarized in this section. The Mn concentration dependence of the lattice parameters of ε-martensite, specifically the parameters a and c, is expressed by the following empirical equations.[103]

$$a(\text{Å}) = 2.517 + 8.886\times10^{-4}\, x_{\text{Mn}}, \quad \text{..... (5)}$$

$$c(\text{Å}) = 4.065 + 12.3\times10^{-4}\, x_{\text{Mn}}, \quad \text{..... (6)}$$

where x_{Mn} is Mn concentration in at%. Based on Eqs. (5) and (6) coupled with other systematic reports on lattice parameters in ternary systems,[103–107] the chemical composition dependence of c/a in Fe–Mn binary alloys and Fe-17~18Mn-xM ternary alloys is displayed in **Fig. 21**, which

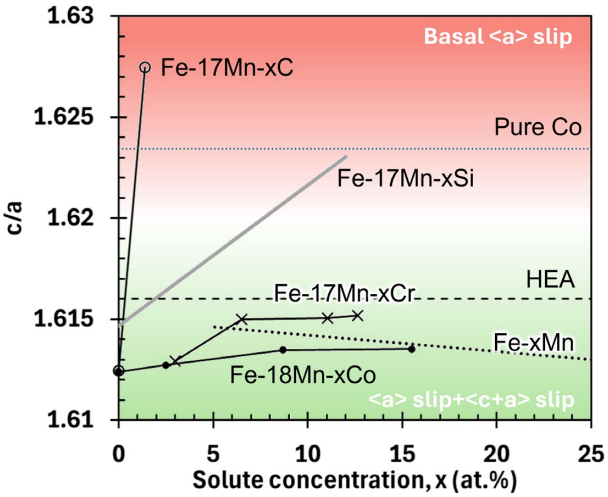

Fig. 21. Dependence of c/a ratio of ε-martensite on solute concentration x in binary Fe-xMn,[103] Fe-17Mn-xC,[104] Fe-17Mn-xSi,[105] Fe-17Mn-xCr,[106] Fe-18Mn-xCo[107] alloys. The line for the Fe-17Mn-xC alloy was estimated from an X-ray diffraction profile of an Fe-17Mn-0.3C alloy (mass%) after immersion into liquid nitrogen.[104] The c/a ratios of pure Co (average of 11 data)[103] and the HEA (Fe-30Mn-10Cr-10Co (at.%))[42] are also plotted for reference. (Online version in color.)

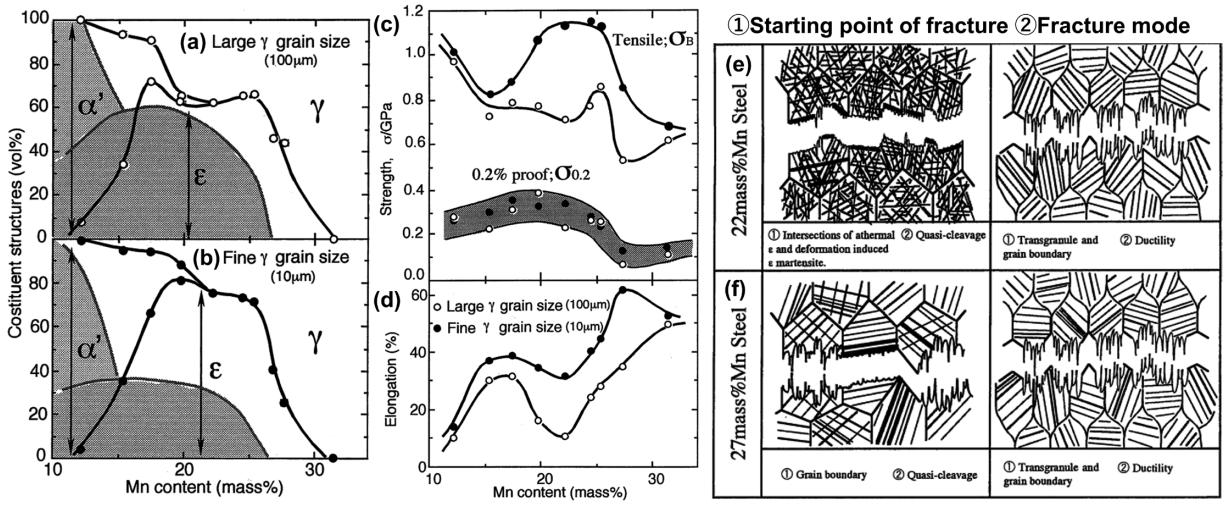

Fig. 20. (a, b) Grain size effect on constituent phase fractions before and after tensile fracture at ambient temperature. Mn content dependence of (c) strength and (d) elongation with different grain sizes in binary Fe–Mn alloys. The hatched areas show the fraction of thermally induced ε and α'-martensite (e, f) Schematic illustrations for the grain size effects on ε-martensite-related damage evolution: examples of Fe-22Mn and Fe-27Mn alloys.[13] Reproduced with permission from reference.[13]

is superimposed on the color map of the active slip system in HCP structures, as shown in Fig. 8(c). As shown in Figs. 10 and 15, the Si and C play critical effects on ductility, which is still an unresolved problem. The chemical composition dependence of *c*/*a* may provide a potential solution to this problem. Mn, C, and Co, which are constituent elements of the ductile metastable HEA introduced earlier, have only a small effect on *c*/*a*. Therefore, all *c*/*a* values in the Fe–Mn binary, Fe–Mn–Cr, and Fe–Mn–Co alloys lie within the green region, where non-basal slip is allowed in terms of lattice parameters. In contrast, Si and C substantially increase *c*/*a*, moving the value into the red region, where non-basal slip is restricted. The effect of lattice parameters still requires further investigation but is expected to serve as a pathway for obtaining damage-resistant high-Mn steel with ε-martensite.

6.3. Designing Reverse Transformability

When the stress accommodation capability of ε-martensite is low, as observed in Fe–Mn–C and Fe–Mn–Si alloy systems, it becomes a critical factor that reduces ductility due to quasi-cleavage fracture. However, the presence of ε-martensite with low stress accommodation capability can strongly hinder dislocation motion, thereby increasing yield strength.[104] **Figure 22**(a) illustrates the temperature dependence of 0.2% proof stress in Fe-17Mn-0.3C steel specimens, both with and without pre-cooling to 77 K, a temperature significantly lower than the starting temperature for γ-ε martensitic transformation (M_s). In the temperature range where martensitic transformation occurs at yielding stress, yield strength increases with decreasing temperature due to the suppression of the thermal activation process of dislocation motion. When martensitic transformation occurs at yielding stress, yield strength decreases with decreasing temperature due to an increase in the chemical driving force, $\Delta G^{\gamma\rightarrow\varepsilon}$. The peak temperature of 0.2% proof stress is referred to as M_S^σ. When the specimen is cooled to 77 K, the 0.2% proof stress increases due to thermally induced γ-ε martensitic transformation. This strengthening effect persists in the temperature range below the starting temperature for the ε-γ reverse transformation (A_s). As introduced in Section 3.1 and shown in Fig. 22(b), the presence of ε-martensite significantly deteriorates elongation when the deformation temperature is below the equilibrium temperature of the γ and ε phases (T_0). When the deformation temperature is higher than T_0, elongation recovers due to deformation-induced ε-γ reverse transformation (the lowest temperature for the ε-γ reverse transformation is referred to as A_d). Thus, the Fe-17Mn-0.3C steel, precooled below M_s shows relatively high yield strength without a deterioration in elongation in the temperature range between A_d and A_s. The relationship among strengthening, elongation, and transformation temperatures is summarized in Fig. 22(c). Because reversibility also affects intersection mechanisms, as mentioned in Section 2, the design of reverse transformability in ε-martensite can provide a new pathway for developing damage-tolerant, high-strength steels.

From the perspective of reverse transformation, deformation-induced reversible $\gamma\leftrightarrow\varepsilon$ transformation plays a significant role in low-cycle fatigue, as briefly introduced in Section 4. The details of reversible microstructure evolution under cyclic loading and the associated low-cycle fatigue properties have been comprehensively reviewed elsewhere.[69] Therefore, this section will briefly highlight three important factors for the mechanical reversibility design. First, γ slip and α'-martensite formation must be avoided, as these plasticity modes are mechanically irreversible (**Fig. 23**(a)). Consequently, BCC phase stability must also be considered in the alloy design.[69] Second, the optimal target temperature is not M_S^σ and lies between M_S^σ and M_d, which is the highest temperature for deformation-induced γ-ε martensitic transformation (Fig. 23(b)).[108,109] Third, according to systematic thermodynamic analysis, the reversible transformation most significantly contributes to fatigue lives when $\Delta G^{\gamma\rightarrow\varepsilon}$ is close to zero, which is consistent with both the chemical composition dependence and temperature dependence of fatigue life (Fig. 23(c)).[108,109] This concept is also applicable to the temperature dependence of fatigue crack growth rates in Fe-30Mn-10Cr-10Co HEA.[110] With recent studies providing mature thermodynamic data for the γ and ε phases,[108,111,112] the free energy-based design of mechanical reversibility enables the exploration of previously unexamined composition and temperature ranges for fatigue-resistant steels.

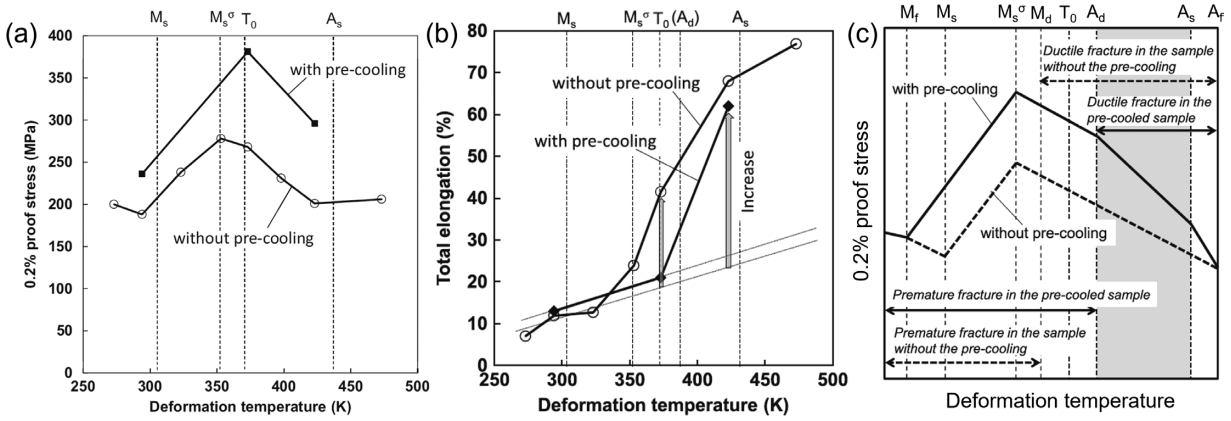

Fig. 22. Temperature dependence of (a) 0.2% proof stress and (b) total elongation with and without pre-cooling in the Fe-17Mn-0.3C steel. (c) Schematic illustration for the temperature dependence of yield strength with and without pre-cooling.[104] Reproduced with permission from reference.[104]

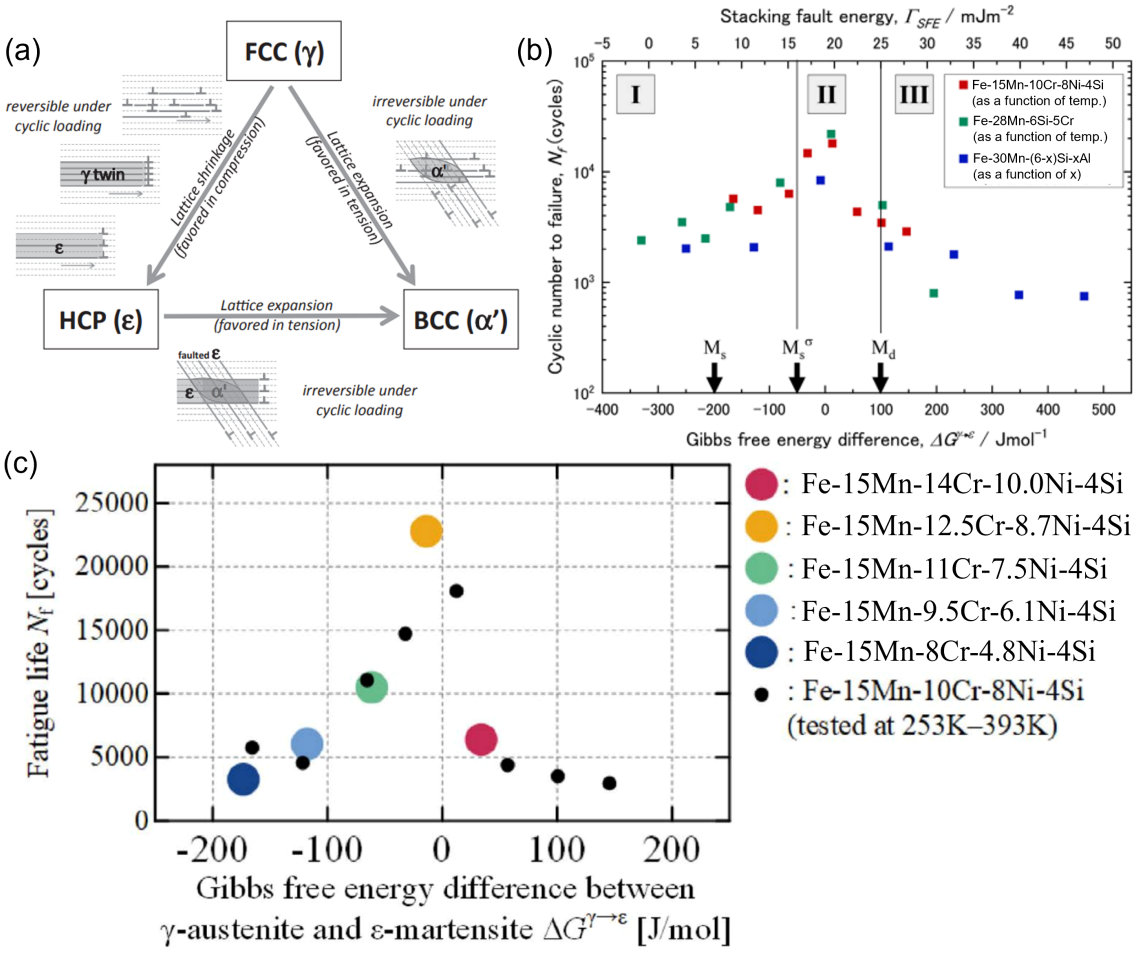

Fig. 23. (a) Schematic illustration for transformation effects on slip reversibility under cyclic loading.[69] Gibbs free energy dependence of fatigue life at a total strain range of 2% in (b) Fe-15Mn-10Cr-8Ni-4Si, Fe-28Mn-6Si-5Cr, Fe-30Mn-(6-x)-xAl,[108] and (c) Fe-15Mn-xCr-yNi-4Si alloys.[109] Reproduced with permission from references[69,108] and with CC license from reference.[109] (Online version in color.)

7. Concluding Remarks

ε-martensite has historically been recognized as a problematic microstructure that causes damage evolution due to the plastic anisotropy and crystallographic orientation relationship between the martensite and the matrix. However, it can endow a shape memory effect and impact high work hardening capability. Additionally, Recent studies have revealed that ε-martensite significantly enhances low-cycle fatigue resistance and does not cause damage evolution in certain specific chemical compositions and deformation temperatures. The key factors contributing to the mechanical superiority of ε-martensite are the plastic isotropy of the intersection microstructure, the elemental or crystallographic heterogeneity of phase stability that enables microcrack arrest, and reverse transformation that prevents stress concentration and fatigue damage accumulation. More specifically, ductile and fatigue-resistant ε-martensite can be designed by optimizing grain size (below 10 μm), lattice parameters (around c/a = 1.61–1.62), and free energy control ($\Delta G^{\gamma\to\varepsilon} \approx 0$). Furthermore, when considering the maximization of fatigue resistance and the mitigation of hydrogen embrittlement, phase stability of the BCC phase must also be addressed. This is because the formation of α'-martensite undermines the reversibility of ε-martensite and reduces its resistance to hydrogen embrittlement.

Although the recent advances in microstructural and mechanical studies of medium Mn steels,[113–115] high Mn[69,116–118] steels, and HEAs[46,119–122] have substantially contributed to the progress of the alloy and microstructure design of ε-martensite, it remains an area under development. For instance, regarding multi-phase microstructures, the stability of the HCP phase and its associated kinetics in retained austenite have not yet been quantitatively designed, but they are likely to become key technologies for the practical use of ε-martensite, because stabilizing the HCP phase generally requires high-alloy compositions. The frontiers of ε-martensite research are expected to pave the way for the creation of new, multi-functional, environmentally robust, and fatigue-resistant high-strength steels.

Statement for Conflict of Interest

The authors declare no conflicts of interest regarding this manuscript.

REFERENCES

1) T. Omori, R. Kainuma and T. Sawaguchi: Ferrous Shape Memory Alloys, in: F.G. Caballero, ed., Encyclopedia of Materials: Metals and Alloys, Elsevier, Oxford, (2022), 214.
2) I. Tamura: *Tetsu-to-Hagané*, **56** (1970), 429 (in Japanese). https://doi.org/10.2355/tetsutohagane1955.56.3_429
3) G.B. Olson and M. Azrin: *Metall. Trans. A*, **9** (1978), 713. https://doi.org/10.1007/BF02659928
4) O. Bouaziz, S. Allain, C.P. Scott, P. Cugy and D. Barbier: *Current*

Opinion in Solid State and Materials Science, **15** (2011), 141. https://doi.org/10.1016/j.cossms.2011.04.002
5) M. Koyama: *Encyclopedia of Materials: Metals and Alloys*, **2** (2022), 95. https://doi.org/10.1016/b978-0-12-819726-4.00067-3
6) Y. Tomota, H. Tokuda, Y. Adachi, M. Wakita, N. Minakawa, A. Moriai and Y. Morii: *Acta Mater.*, **52** (2004), 5737. https://doi.org/10.1016/j.actamat.2004.08.016
7) S. Harjo, N. Tsuchida, J. Abe and W. Gong: *Sci. Rep.*, **7** (2017), 15149. https://doi.org/10.1038/s41598-017-15252-5
8) M. Koyama, T. Sawaguchi and K. Tsuzaki: *Mater. Sci. Eng. A*, **528** (2011), 2882. https://doi.org/10.1016/j.msea.2010.12.065
9) A. Sato, K. Soma and T. Mori: *Acta Metall.*, **30** (1982), 1901. https://doi.org/10.1016/0001-6160(82)90030-X
10) Z. Nishiyama: Martensitic Transformation, Elsevier, (2012), 49.
11) Y. Tomota, M. Strum and J.W. Morris: *Metall. Trans. A*, **17** (1986), 537. https://doi.org/10.1007/BF02643961
12) T. Sawaguchi, I. Nikulin, K. Ogawa, K. Sekido, S. Takamori, T. Maruyama, Y. Chiba, A. Kushibe, Y. Inoue and K. Tsuzaki: *Scripta Mater.*, **99** (2015), 49. https://doi.org/10.1016/j.scriptamat.2014.11.024
13) H. Nakatsu and S. Takaki: *J. Japan Inst Metals*, **60** (1996), 141 (in Japanese). https://doi.org/10.2320/jinstmet1952.60.2_141
14) M. Koyama, S. Okazaki, T. Sawaguchi and K. Tsuzaki: *Metall. Mater. Trans. A*, **47** (2016), 2656. https://doi.org/10.1007/s11661-016-3431-9
15) H. Li, M. Koyama, T. Sawaguchi, K. Tsuzaki and H. Noguchi: *Philos. Mag. Lett.*, **95** (2015), 303. https://doi.org/10.1080/09500839.2015.1052029
16) M. Koyama, H. Noguchi and K. Tsuzaki: Microstructural Crack Tip Plasticity Controlling Small Fatigue Crack Growth, The Plaston Concept, Springer, Singapore, (2022), 213.
17) T. Sawaguchi, P. Sahu, T. Kikuchi, K. Ogawa, S. Kajiwara, A. Kushibe, M. Higashino and T. Ogawa: *Scripta Mater.*, **54** (2006), 1885. https://doi.org/10.1016/j.scriptamat.2006.02.013
18) T. Sawaguchi, L.-G. Bujoreanu, T. Kikuchi, K. Ogawa, M. Koyama and M. Murakami: *Scripta Mater.*, **59** (2008), 826. https://doi.org/10.1016/j.scriptamat.2008.06.030
19) T. Sawaguchi, Y. Tomota, F. Yoshinaka and S. Harjo: *Acta Mater.*, **242** (2023), 118494. https://doi.org/10.1016/j.actamat.2022.118494
20) H. Nakatsu, T. Miyata and S. Takaki: *J. Japan Inst. Metals*, **60** (1996), 928 (in Japanese). https://doi.org/10.2320/jinstmet1952.60.10_928
21) M. Koyama, T. Sawaguchi and K. Tsuzaki: *Metall. Mater. Trans. A*, **43A** (2012), 4063. https://doi.org/10.1007/s11661-012-1220-7
22) Y.-B. Ju, M. Koyama, T. Sawaguchi, K. Tsuzaki and H. Noguchi: *Int. J. Fatigue*, **103** (2017), 533. https://doi.org/10.1016/j.ijfatigue.2017.06.040
23) K. Sekido, T. Ohmura, T. Sawaguchi, M. Koyama, H.W. Park and K. Tsuzaki: *Scripta Mater.*, **65** (2011), 942. https://doi.org/10.1016/j.scriptamat.2011.08.010
24) T. Maruyama, T. Kurita, S. Kozaki, K. Andou, S. Farjami and H. Kubo: *Mater Sci Tech-Lond*, **24** (2008), 908. https://doi.org/10.1179/174328408X302585
25) J.A. Venables: *Philos. Mag. A*, **7** (1962), 35. https://doi.org/10.1080/14786436208201856
26) G.B. Olson and M. Cohen: *Metallurgical Transactions A*, **6** (1975), 791. https://doi.org/10.1007/BF02672301
27) D. Singh, W. Tasaki, F. Yoshinaka, S. Takamori, S. Emura, K. Tsuchiya and T. Sawaguchi: *Materials Charact.*, **205** (2023), 113358. https://doi.org/10.1016/j.matchar.2023.113358
28) Y. Wada, N. Nakada and S. Onaka: *ISIJ Int.*, **62** (2022), 613. https://doi.org/10.2355/isijinternational.ISIJINT-2021-425
29) A.J. Bogers and W.G. Burgers: *Acta Metall.*, **12** (1964), 255. https://doi.org/10.1016/0001-6160(64)90194-4
30) G.B. Olson and M. Cohen: *Metall. Trans. A*, **7** (1976), 1905. https://doi.org/10.1007/BF02659823
31) G.B. Olson and M. Cohen: *J. Less-Common Met.*, **28** (1972), 107. https://doi.org/10.1016/0022-5088(72)90173-7
32) L. Zhang, M. Wen, M. Imade, S. Fukuyama and K. Yokogawa: *Acta Mater.*, **56** (2008), 3414. https://doi.org/10.1016/j.actamat.2008.03.022
33) F. Yoshinaka, T. Sawaguchi, S. Takamori, S. Emura and Y. Inoue: *Int. J. Fatigue*, **171** (2023), 107581. https://doi.org/10.1016/j.ijfatigue.2023.107581
34) J.H. Yang and C.M. Wayman: *Acta Metall. Mater.*, **40** (1992), 2025. https://doi.org/10.1016/0956-7151(92)90188-K
35) S. Matsumoto, A. Sato and T. Mori: *Acta Metall. Mater.*, **42** (1994), 1207. https://doi.org/10.1016/0956-7151(94)90137-6
36) X. Zhang and T. Sawaguchi: *Acta Mater.*, **143** (2018), 237. https://doi.org/10.1016/j.actamat.2017.10.009
37) X. Zhang, T. Sawaguchi, K. Ogawa, F. Yin and X. Zhao: *J. Alloys Compounds*, **577** (2013), S533. https://doi.org/10.1016/j.jallcom.2011.12.109
38) Y.-K. Lee: *Metall. Mater. Trans. A*, **32** (2001), 229. https://doi.org/10.1007/s11661-001-0253-0
39) X. Zhang, T. Sawaguchi, K. Ogawa, F. Yin and X. Zhao: *Philos. Mag.*, **91** (2011), 4410. https://doi.org/10.1080/14786435.2011.608734
40) F. Yoshinaka, T. Sawaguchi, S. Takamori and S. Emura: *Mater. Sci. Eng. A*, **833** (2022), 142583. https://doi.org/10.1016/j.msea.2021.142583
41) A.W. Sleeswyk: *Philos. Mag. A*, **7** (1962), 1597. https://doi.org/10.1080/14786436208213294
42) Y. Bu, Z. Li, J. Liu, H. Wang, D. Raabe and W. Yang: *Phys. Rev. Lett.*, **122** (2019), 075502. https://doi.org/10.1103/PhysRevLett.122.075502
43) T. Eguchi, M. Koyama, Y. Fukushima, C.C. Tasan and K. Tsuzaki: *Procedia Structural Integrity*, **13** (2018), 831. https://doi.org/10.1016/j.prostr.2018.12.159
44) K. Ichii, M. Koyama, C.C. Tasan and K. Tsuzaki: *Procedia Structural Integrity*, **13** (2018), 716. https://doi.org/10.1016/j.prostr.2018.12.119
45) Z. Li, K.G. Pradeep, Y. Deng, D. Raabe and C.C. Tasan: *Nature*, **534** (2016), 227. https://doi.org/10.1038/nature17981
46) Z.M. Li, C.C. Tasan, K.G. Pradeep and D. Raabe: *Acta Mater.*, **131** (2017), 323. https://doi.org/10.1016/j.actamat.2017.03.069
47) N. Bergeon, G. Guenin and C. Esnouf: *Mater. Sci. Eng. A*, **242** (1998), 77. https://doi.org/10.1016/S0921-5093(97)00511-X
48) S. Takaki, T. Furuya and Y. Tokunaga: *ISIJ Int.*, **30** (1990), 632. https://doi.org/10.2355/isijinternational.30.632
49) M. Koyama, T. Sawaguchi and K. Tsuzaki: *Materi. Trans.*, **53** (2012), 546. https://doi.org/10.2320/matertrans.M2011342
50) M. Koyama, T. Sawaguchi and K. Tsuzaki: *Tetsu-to-Hagané*, **104** (2018), 187 (in Japanese). https://doi.org/10.2355/tetsutohagane.TETSU-2017-089
51) M. Koyama, T. Sawaguchi and K. Tsuzaki: *ISIJ Int.*, **58** (2018), 1383. https://doi.org/10.2355/isijinternational.ISIJINT-2018-237
52) M. Koyama, T. Sawaguchi and K. Tsuzaki: *ISIJ Int.*, **52** (2012), 161. https://doi.org/10.2355/isijinternational.52.161
53) S. Mahajan and G.Y. Chin: *Acta Metall.*, **21** (1973), 173. https://doi.org/10.1016/0001-6160(73)90059-X
54) L. Rémy: *Metall. Trans. A*, **12** (1981), 387. https://doi.org/10.1007/BF02648536
55) T. Kaneko, M. Koyama, T. Fujisawa and K. Tsuzaki: *Tetsu-to-Hagané*, **102** (2016), 227 (in Japanese). https://doi.org/10.2355/tetsutohagane.TETSU-2015-081
56) T. Kaneko, M. Koyama, T. Fujisawa and K. Tsuzaki: *ISIJ Int.*, **56** (2016), 2037. https://doi.org/10.2355/isijinternational.ISIJINT-2016-272
57) N. Uehata, M. Koyama, S. Takagi and K. Tsuzaki: *ISIJ Int.*, **58** (2018), 179. https://doi.org/10.2355/isijinternational.ISIJINT-2017-468
58) C.C. Tasan, J.P.M. Hoefnagels and M.G.D. Geers: *Acta Mater.*, **60** (2012), 3581. https://doi.org/10.1016/j.actamat.2012.03.017
59) M. Koyama, C.C. Tasan, E. Akiyama, K. Tsuzaki and D. Raabe: *Acta Mater.*, **70** (2014), 174. https://doi.org/10.1016/j.actamat.2014.01.048
60) T. Kumamoto, M. Koyama, K. Sato and K. Tsuzaki: *Mater. Trans.*, **60** (2019), 2368. https://doi.org/10.2320/matertrans.MT-M2019196
61) M. Koyama: *Accounts of Materials Research*, **2** (2021), 1167. https://doi.org/10.1021/accountsmr.1c00160
62) R. Ueji, Y. Takagi, N. Tsuchida, K. Shinagawa, Y. Tanaka and T. Mizuguchi: *Mater. Sci. Eng. A*, **576** (2013), 14. https://doi.org/10.1016/j.msea.2013.03.071
63) A. Das: *Metall. Mater. Trans. A*, **47** (2016), 748. https://doi.org/10.1007/s11661-015-3266-9
64) Y.K. Lee, S.J. Lee and J. Han: *Mater Sci Tech-Lond*, **32** (2016), 1. https://doi.org/10.1080/02670836.2015.1114252
65) K. Tsuzaki, Y. Natsume, Y. Tomota and T. Maki: *Scripta Metall. Mater.*, **33** (1995), 1087. https://doi.org/10.1016/0956-716X(95)00337-U
66) M. Koyama, T. Sawaguchi and K. Tsuzaki: *Mater. Trans.*, **56** (2015), 819. https://doi.org/10.2320/matertrans.M2015042
67) M. Koyama, T. Kaneko, T. Sawaguchi and K. Tsuzaki: *Int. J. Frac.*, **213** (2018), 193. https://doi.org/10.1007/s10704-018-0307-6
68) Y.-B. Ju, M. Koyama, T. Sawaguchi, K. Tsuzaki and H. Noguchi: *Acta Mater.*, **112** (2016), 326. https://doi.org/10.1016/j.actamat.2016.04.042
69) T. Sawaguchi, T. Maruyama, H. Otsuka, A. Kushibe, Y. Inoue and K. Tsuzaki: *Mater. Trans.*, **57** (2016), 283. https://doi.org/10.2320/matertrans.MB201510
70) K. Ogawa, T. Sawaguchi, T. Kikuchi, M. Koyama and M. Murakami: Proceedings of the International Conference on Shape Memory and Superelastic Technologies, SMST-2007, (2008), 645.
71) K.H. So, J.S. Kim, Y.S. Chun, K.-T. Park, Y.-K. Lee and C.S. Lee: *ISIJ Int.*, **49** (2009), 1952. https://doi.org/10.2355/isijinternational.49.1952
72) Y.S. Chun, K.-T. Park and C.S. Lee: *Scripta Mater.*, **66** (2012), 960. https://doi.org/10.1016/j.scriptamat.2012.02.038
73) M. Koyama, E. Akiyama, Y.-K. Lee, D. Raabe and K. Tsuzaki: *Int. J. Hydrog. Energy*, **42** (2017), 12706. https://doi.org/10.1016/j.ijhydene.2017.02.214
74) S.M. Teus, V.N. Shyvanyuk and V.G. Gavriljuk: *Mater. Sci. Eng. A*, **497** (2008), 290. https://doi.org/10.1016/j.msea.2008.07.003

75) Y.S. Chun, J.S. Kim, K.-T. Park, Y.-K. Lee and C.S. Lee: *Mater. Sci. Eng. A*, **533** (2012), 87. https://doi.org/10.1016/j.msea.2011.11.039
76) S.-M. Lee, I.-J. Park, J.-G. Jung and Y.-K. Lee: *Acta Mater.*, **103** (2016), 264. https://doi.org/10.1016/j.actamat.2015.10.015
77) M. Koyama, N. Terao and K. Tsuzaki: *Mater. Lett.*, **249** (2019), 197. https://doi.org/10.1016/j.matlet.2019.04.093
78) Y. Wen, M. Koyama, T. Hojo, S. Ajito and E. Akiyama: *ISIJ Int.*, **64** (2024), 474. https://doi.org/10.2355/isijinternational.ISIJINT-2023-130
79) M. Koyama, S. Iikubo and R.S. Varanasi: *ISIJ Int.*, **64** (2024), 732. https://doi.org/10.2355/isijinternational.ISIJINT-2023-243
80) M. Koyama, T. Ogawa, D. Yan, Y. Matsumoto, C.C. Tasan, K. Takai and K. Tsuzaki: *Int. J. Hydrog. Energy*, **42** (2017), 26423. https://doi.org/10.1016/j.ijhydene.2017.08.209
81) T.P. Perng and C.J. Altstetter: *Metall. Trans. A*, **18** (1987), 123. https://doi.org/10.1007/BF02646229
82) C. Hao, M. Koyama and E. Akiyama: *Metall. Mater. Trans. A*, **51** (2020), 6184. https://doi.org/10.1007/s11661-020-06021-7
83) I.M. Robertson, P. Sofronis, A. Nagao, M.L. Martin, S. Wang, D.W. Gross and K.E. Nygren: *Metall. Mater. Trans. A*, **46** (2015), 2323. https://doi.org/10.1007/s11661-015-2836-1
84) M. Koyama, S.M. Taheri-Mousavi, H. Yan, J. Kim, B.C. Cameron, S.S. Moeini-Ardakani, J. Li and C.C. Tasan: *Science Advances*, **6** (2020), eaaz1187. https://doi.org/10.1126/sciadv.aaz1187
85) M.S. Hasan, M.F. Kapci, B. Bal, M. Koyama, H. Bayat and W. Xu: *Int. J. Hydrog. Energy*, **57** (2024), 60. https://doi.org/10.1016/j.ijhydene.2023.12.274
86) P. Sofronis and R.M. McMeeking: *J. Mech. Phys. Solids*, **37** (1989), 317. https://doi.org/10.1016/0022-5096(89)90002-1
87) J. Lufrano and P. Sofronis: *Acta Mater.*, **46** (1998), 1519. https://doi.org/10.1016/S1359-6454(97)00364-9
88) M. Wang, E. Akiyama and K. Tsuzaki: *Corros. Sci.*, **48** (2006), 2189. https://doi.org/10.1016/j.corsci.2005.07.010
89) Y. Shibayama, T. Hojo, M. Koyama and E. Akiyama: *Int. J. Hydrog. Energy*, **88** (2024), 1010. https://doi.org/10.1016/j.ijhydene.2024.09.123
90) M. Koyama, M. Rohwerder, C.C. Tasan, A. Bashir, E. Akiyama, K. Takai, D. Raabe and K. Tsuzaki: *Mater Sci Tech-Lond*, **33** (2017), 1481. https://doi.org/10.1080/02670836.2017.1299276
91) S. Ajito, H. Kakinuma, M. Koyama and E. Akiyama: *Mater. Trans.*, **65** (2024), 1436. https://doi.org/10.2320/matertrans.MT-C2024008
92) C. Hao, M. Koyama, S. Ajito and E. Akiyama: *Int. J. Hydrog. Energy*, **46** (2021), 27221. https://doi.org/10.1016/j.ijhydene.2021.05.162
93) K. Ichii, M. Koyama, C.C. Tasan and K. Tsuzaki: *Ecf22 - Loading and Environmental Effects on Structural Integrity*, **13** (2018), 716. https://doi.org/10.1016/j.prostr.2018.12.119
94) K. Ichii, M. Koyama, C.C. Tasan and K. Tsuzaki: *Scripta Mater.*, **150** (2018), 74. https://doi.org/10.1016/j.scriptamat.2018.03.003
95) M. Koyama, Y. Abe and K. Tsuzaki: *ISIJ Int.*, **58** (2018), 1745. https://doi.org/10.2355/isijinternational.ISIJINT-2018-260
96) Y. Bai, Y. Momotani, M.C. Chen, A. Shibata and N. Tsuji: *Mater. Sci. Eng. A*, **651** (2016), 935. https://doi.org/10.1016/j.msea.2015.11.017
97) N. Kobayashi, M. Koyama, M. Yamamura, T. Hojo and E. Akiyama: *J. Japan Inst. Met. Mater.*, **86** (2022), 77 (in Japanese). https://doi.org/10.2320/jinstmet.J2021054
98) N. Kobayashi, M. Koyama, K. Kobayashi, T. Hojo and E. Akiyama: *Mater. Trans.*, **63** (2022), 247. https://doi.org/10.2320/matertrans.MT-M2021170
99) T. Onomoto, Y. Terazawa, T. Tsuchiyama and S. Takaki: *ISIJ Int.*, **49** (2009), 1246. https://doi.org/10.2355/isijinternational.49.1246
100) E.O. Hall: *Proc. Phys. Soc. Sect. B*, **64** (1951), 747. https://doi.org/10.1088/0370-1301/64/9/303
101) J. Petch N.: *J. Iron Steel Inst.*, **174** (1953), 25.
102) J.D. Eshelby, F.C. Frank and F.R.N. Nabarro: *The London, Edinburgh, and Dublin Philosophical Magazine and Journal of Science*, **42** (1951), 351. https://doi.org/10.1080/14786445108561060
103) P. Marinelli, A. Baruj, A.F. Guillermet and M. Sade: *Z. Metallkunde*, **92** (2001), 489.
104) M. Koyama, T. Sawaguchi and K. Tsuzaki: *Mater. Sci. Eng. A*, **556** (2012), 331. https://doi.org/10.1016/j.msea.2012.06.095
105) J. Martínez, G. Aurelio, G.J. Cuello, S.M. Cotes and J. Desimoni: *Mater. Sci. Eng. A*, **437** (2006), 323. https://doi.org/10.1016/j.msea.2006.08.014
106) F. Malamud, L.M. Guerrero, P. La Roca, M. Sade and A. Baruj: *Materials & Design*, **139** (2018), 314. https://doi.org/10.1016/j.matdes.2017.11.017
107) P. Marinelli, M. Sade and A. Fernández Guillermet: *Scripta Mater.*, **46** (2002), 805. https://doi.org/10.1016/S1359-6462(02)00080-5
108) T. Sawaguchi, I. Nikulin, K. Ogawa, S. Takamori, F. Yoshinaka, Y. Chiba, H. Otsuka, Y. Inoue and A. Kushibe: *Acta Mater.*, **220** (2021), 117267. https://doi.org/10.1016/j.actamat.2021.117267
109) F. Yoshinaka, Y. Tsutsumi, T. Nagira, S. Takamori, S. Emura, T. Sawaguchi, H. Katayama, T. Nakamura, Y. Inoue, S. Motomura and A. Kushibe: *ISIJ Int.*, **64** (2024), 1197. https://doi.org/10.2355/isijinternational.ISIJINT-2023-437
110) M. Koyama, T. Eguchi and K. Tsuzaki: *ISIJ Int.*, **61** (2021), 641. https://doi.org/10.2355/isijinternational.ISIJINT-2020-504
111) Y.-K. Lee and C. Choi: *Metall. Mater. Trans. A*, **31** (2000), 355. https://doi.org/10.1007/s11661-000-0271-3
112) A. Saeed-Akbari, J. Imlau, U. Prahl and W. Bleck: *Metall. Mater. Trans. A*, **40** (2009), 3076. https://doi.org/10.1007/s11661-009-0050-8
113) Y.K. Lee and J. Han: *Mater Sci Tech-Lond*, **31** (2015), 843. https://doi.org/10.1179/1743284714y.0000000722
114) G. Su, X. Gao, T. Yan, D. Zhang, C. Cui, L. Du, Z. Liu, Y. Tang and J. Hu: *Mater. Sci. Eng. A*, **736** (2018), 417. https://doi.org/10.1016/j.msea.2018.08.082
115) M. Koyama, T. Yamashita, S. Morooka, T. Sawaguchi, Z.P. Yang, T. Hojo, T. Kawasaki and S. Harjo: *ISIJ Int.*, **62** (2022), 2036. https://doi.org/10.2355/isijinternational.ISIJINT-2021-510
116) P. Chowdhury, D. Canadinc and H. Sehitoglu: *Mater. Sci. Eng. R*, **122** (2017), 1. https://doi.org/10.1016/j.mser.2017.09.002
117) J.-B. Seol, J.E. Jung, Y.W. Jang and C.G. Park: *Acta Mater.*, **61** (2013), 558. https://doi.org/10.1016/j.actamat.2012.09.078
118) Q. Lai, S. Chang, Y. Wei, S. Wu, P. Jacques, T. Pardoen and G. Fan: *Mater. Res. Lett.*, **12** (2024), 700. https://doi.org/10.1080/21663831.2024.2372082
119) S. Wei, F. He and C.C. Tasan: *J. Mater. Res.*, **33** (2018), 2924. https://doi.org/10.1557/jmr.2018.306
120) S.S. Nene, M. Frank, K. Liu, R.S. Mishra, B.A. McWilliams and K.C. Cho: *Sci. Rep.*, **8** (2018), 9920. https://doi.org/10.1038/s41598-018-28383-0
121) M. Koyama, T. Gondo and K. Tsuzaki: *Metals*, **11** (2021), 742. https://doi.org/10.3390/met11050742
122) X. Wang, R.R. De Vecchis, C. Li, H. Zhang, X. Hu, S. Sridar, Y. Wang, W. Chen and W. Xiong: *Science Adv.*, **8** (2022), eabo7333. https://doi.org/10.1126/sciadv.abo7333